

แบบจำลองของการลดลงของรังสีคอสมิกแบบเฟอร์มิ



นางสาวกนกพร สิริรุ่งนาวรัตน์

สถาบันวิทยบริการ

จุฬาลงกรณ์มหาวิทยาลัย

วิทยานิพนธ์นี้เป็นส่วนหนึ่งของการศึกษาตามหลักสูตรปริญญาวิทยาศาสตรดุษฎีบัณฑิต

สาขาวิชาฟิสิกส์ ภาควิชาฟิสิกส์


คณะวิทยาศาสตร์ จุฬาลงกรณ์มหาวิทยาลัย

ปีการศึกษา 2547

ISBN 974-17-6025-6

ลิขสิทธิ์ของจุฬาลงกรณ์มหาวิทยาลัย

MODELING OF FORBUSH DECREASES IN COSMIC RAYS



Miss Kanokporn Leerunnavarat

สถาบันวิทยบริการ  
จุฬาลงกรณ์มหาวิทยาลัย

A Dissertation Submitted in Partial Fulfillment of the Requirements  
for the Degree of Doctor of Philosophy in Physics

Department of Physics

Faculty of Science

Chulalongkorn University

Academic year 2004

ISBN 974-17-6025-6

Thesis Title	MODELING OF FORBUSH DECREASES IN COSMIC RAYS
By	MISS KANOKPORN LEERUNGNAVARAT
Filed of study	Physics
Thesis Advisor	Sojiphong Chatraphorn, Ph.D.
Thesis Co-advisor	Associate Professor David Ruffolo, Ph.D.

---

Accepted by the Faculty of Science, Chulalongkorn University in Partial Fulfillment of the Requirements for the Doctor's Degree

.....Dean of the Faculty of Science  
(Professor Piamsak Menasveta, Ph.D.)

THESIS COMMITTEE

..... Chairman  
(Ahpisit Ungkitchanukit, Ph.D.)

..... Thesis Advisor  
(Sojiphong Chatraphorn, Ph.D.)

..... Thesis Co-advisor  
(Associate Professor David Ruffolo, Ph.D.)

..... Member  
(Assistant Professor Kajornyod Yoodee, Ph.D.)

..... Member  
(Assistant Professor Udomsilp Pinsook, Ph.D.)

..... Member  
(Patcha Chatraphorn, Ph.D.)

..... Member  
(Nuanwan Sanguansak, Ph.D.)

นางสาวกนกพร ลิ้รุ่งนาวรัตน์ : แบบจำลองของการลดลงของรังสีคอสมิกแบบฟอรับูช.  
(MODELING OF FORBUSH DECREASES IN COSMIC RAYS) อ. ที่ปรึกษา : อ. ดร.  
โศจิพงษ์ ฉัตรภรณ์, อ.ที่ปรึกษาร่วม : รศ. ดร. เดวิด รูฟโฟโล, 88 หน้า. ISBN 974-17-  
6025-6.

เมื่อดวงอาทิตย์เกิดการปะทุและปลดปล่อยกลุ่มอนุภาคจำนวนมากภายในเวลาอันสั้น เราเรียกกลุ่มอนุภาคเหล่านี้ว่า “coronal mass ejections” (CME) ที่มีความเร็วสูง ซึ่งจะก่อให้เกิดความไม่ต่อเนื่องในลมสุริยะที่เรียกว่า คลื่นกระแทก (shocks) คลื่นกระแทกและรังสีคอสมิกพลังงานสูงสามารถส่งผลกระทบต่อโลกและมนุษย์บนผิวโลกได้ เราเรียกผลกระทบนี้ว่า ผลกระทบเนื่องจากสภาพอวกาศ (space weather effects) ในวิทยานิพนธ์นี้ได้ศึกษาการชนส่งอนุภาคในบริเวณใกล้หน้าคลื่นกระแทก (บริเวณที่เกิด loss cone precursor) และใกล้หลังคลื่นกระแทก (การลดลงของรังสีคอสมิกแบบฟอรับูชขั้นแรก) โดยจำลองสถานการณ์บริเวณใกล้คลื่นกระแทกซึ่งใช้การคำนวณเชิงตัวเลขแก้สมการการชนส่งอนุภาคต่อเวลา เราพบว่าความกว้างของสัญญาณล่วงหน้าสามารถช่วยพยากรณ์ว่าผลกระทบเนื่องจากสภาพอวกาศที่กำลังจะเกิดขึ้นเกิดจากคลื่นกระแทกชนิดใด ผลการจำลองยังแสดงให้เห็นว่า คลื่นกระแทกชนิดเกือบตั้งฉาก (quasi-perpendicular shock) จะทำให้เกิดการลดลงของอนุภาคกลุ่มที่มีมูมน้อยกว่า 25 องศา ในบริเวณหน้าคลื่นกระแทก และ คลื่นกระแทกชนิดเกือบขนาน (quasi-parallel shock) จะทำให้เกิดการลดลงของอนุภาคกลุ่มที่มีมูมน้อยกว่า 50 องศา ในบริเวณหน้าคลื่นกระแทก จากผลที่ได้แสดงว่าการวัดสัญญาณล่วงหน้าสามารถพยากรณ์ได้ว่าคลื่นกระแทกจะมาถึงโลกและส่งผลกระทบต่อใด เรายังพบอีกว่าการสะท้อนที่คลื่นกระแทกอาจเป็นสาเหตุที่ก่อให้เกิดการลดลงของรังสีคอสมิกแบบฟอรับูชขั้นที่หนึ่ง

สถาบันวิทยบริการ  
จุฬาลงกรณ์มหาวิทยาลัย

ภาควิชาฟิสิกส์  
สาขาวิชาฟิสิกส์  
ปีการศึกษา 2547

ลายมือชื่อนิสิต.....  
ลายมือชื่ออาจารย์ที่ปรึกษา.....  
ลายมือชื่ออาจารย์ที่ปรึกษาร่วม.....

## 4273842423 : MAJOR PHYSICS

KEY WORD: FORBUSH DECREASES / CORONAL MASS EJECTIONS / SHOCKS / COSMIC RAYS

KANOKPORN LEERUNGNARAT : MODELING OF FORBUSH DECREASES IN COSMIC RAYS. THESIS ADVISOR : SOJIPHONG CHATRAPHORN, Ph.D., THESIS COADVISOR : ASSOC. PROF. DAVID RUFFOLO, Ph.D., 88 pp. ISBN 974-17-6025-6.

An explosion at the Sun that releases a large amount of mass with high velocity, known as a coronal mass ejection (CME), causes a discontinuity in the solar wind known as a shock. The shock and associated energetic cosmic rays could cause various problems for human activities known as “space weather effects.” This work studies the particle transport in the region just before the shock (loss cone precursor) and just behind the shock (the first step of Forbush decrease) by modeling and performing time-dependent numerical simulations of GCRs in the vicinity of the shock. We found that the width of the precursor loss cone provides a prediction of whether the approaching shock is quasi-parallel or quasi-perpendicular. We also showed that quasi-perpendicular shocks produce loss cones with opening angles  $\sim 25^\circ$ , whereas quasi-parallel shocks have loss cones with opening angles  $\sim 50^\circ$ . This implies that loss cone measurements can in principle provide a quantitative indication of the time when an interplanetary shock will arrive at Earth. We also found that reflection is a possible mechanism for the first step of the Forbush decrease.

สถาบันวิทยบริการ  
จุฬาลงกรณ์มหาวิทยาลัย

Department Physics

Field of study Physics

Academic year 2004

Student's signature.....

Advisor's signature.....

Co-advisor's signature.....

# Acknowledgments

This work would not have been completed without a lot of help and kindness from the people in the Space Physics and Energetic Particles group. Firstly I would like to give all my eternal thanks and respects to Associate Professor David Ruffolo, my former advisor and current co-advisor, who has been providing me a great deal of help and suggestion. I am always very much grateful. This thesis might not have succeeded without help from: Professor John W. Bieber, who provided neutron monitor data, important suggestions, and hospitality while I was at the University of Delaware; Dr. David Lario, who provided programs to simulate the CME propagation; and Dr. Sojiphong Chatraphorn, my current advisor.

I would like to give my gratitude to my thesis committee, Dr. Ahpisit Ungkitchanukit, Assistant Professor Kajornyod Yoodee, Assistant Professor Udomsilp Pinsook, Dr. Patcha Chatraphorn, and Dr. Nuanwan Sanguansak, for their kind suggestions.

Much help during the work was provided by Miss Piyanate Chuychai, Mr. Paisan Tooprakai, Dr. Tanin Nutaro, Dr. Thiranee Khumlumlert, Dr. Alejandro Sáiz, and Mr. Kittipat Malakit. I appreciate this very much. Thanks to everyone in the SEP group for their all kindness. Finally, I could not have had today without all the support from my parents and family. I do not forget Non, my husband, who always gives me mental support, care, and food.

# Table of Contents

	page
Abstract in Thai .....	iv
Abstract in English .....	v
Acknowledgments .....	vi
Table of Contents .....	vii
List of Figures .....	ix
List of Tables .....	xii
<b>1 Introduction .....</b>	<b>1</b>
<b>2 Theoretical Background .....</b>	<b>5</b>
2.1 Solar Wind and Interplanetary Magnetic Fields .....	5
2.2 Coronal Mass Ejections (CMEs) .....	10
2.3 Cosmic Rays and Their Transport in the Heliosphere .....	13
2.4 Interplanetary Shocks .....	14
2.5 Cosmic Ray Observations during Forbush Decreases .....	16
2.5.1 General Observations in Space and on Earth .....	18
2.5.2 Magnitude .....	21
2.5.3 Rigidity Dependence .....	22
2.5.4 Anisotropy and Precursory Effects .....	25
2.5.5 Recovery Characteristics .....	26
<b>3 Compton-Getting Anisotropies during Forbush Decreases .....</b>	<b>28</b>
<b>4 Loss Cone Precursors and Advance Prediction of Space Weather .....</b>	<b>36</b>
4.1 Forbush Decrease Precursors and Space Weather Effects .....	36

4.2 Model .....	41
4.2.1 Transport Equation .....	41
4.2.2 Numerical Simulations .....	43
4.3 Results .....	45
4.4 Discussion .....	53
4.5 Conclusions .....	57
<b>5 Simulation of Forbush Decreases .....</b>	<b>59</b>
5.1 Transport Equation .....	60
5.2 Numerical Methods .....	62
5.3 Numerical Simulations .....	63
5.3.1 Model I .....	63
5.3.2 Model II .....	66
5.3.3 Program Descriptions .....	67
5.4 Results and Discussion .....	70
<b>References .....</b>	<b>73</b>
<b>Appendices .....</b>	<b>80</b>
<b>Appendix A List of Acronyms .....</b>	<b>81</b>
<b>Appendix B The Relations between <math>F</math>, <math>f</math>, <math>j</math> and <math>N</math> .....</b>	<b>83</b>
<b>Appendix C Operator Splitting Technique .....</b>	<b>86</b>
<b>Vitae .....</b>	<b>88</b>

สถาบันวิทยบริการ  
จุฬาลงกรณ์มหาวิทยาลัย

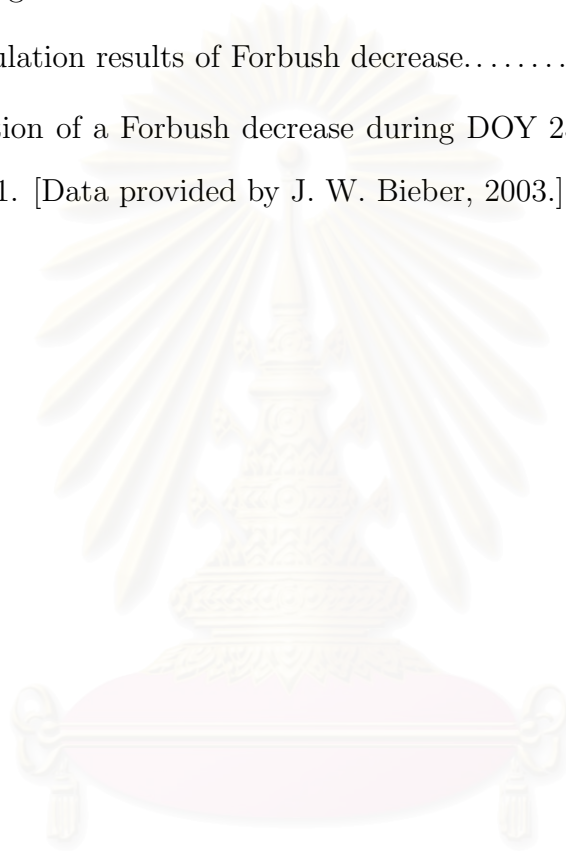


# List of Figures

Figure	Page
2.1 Archimedean spiral interplanetary magnetic field lines in the heliospheric equatorial plane (not to scale).....	6
2.2 A sketch of an interplanetary magnetic field line for higher heliospheric latitudes (not to scale). The magnetic field line wraps around a cone whose surface has an angle $\theta$ with respect to the rotation axis.....	7
2.3 The two-dimensional side view of the HCS.....	9
2.4 A schematic drawing of the heliospheric current sheet (HCS).....	10
2.5 A photograph of a CME taken by the SOHO spacecraft.....	11
2.6 A plausible drawing of a CME [Ihara et al., 2001].....	12
2.7 An illustration of a CME, its driven shock, and interplanetary magnetic fields. ....	15
2.8 Schematic of GCR counts as a function of time as a CME and its shock pass by a detector.....	17
2.9 An illustration of Forbush decreases at two detector locations, A and B. Both detectors observe a first-step FD at the time of shock passage (S). At location A, both the shock and the CME pass the detector. The GCR flux is especially depressed when the ejecta pass by (for $T_1 < T < T_2$ ) [Cane, 2000].....	19
2.10 Various solar wind data as indicators for shocks and CMEs [Gosling et al., 1995].....	20

2.11	A schematic drawing of cosmic rays travelling toward the Earth (dashed lines) in the presence of the geomagnetic field (solid lines) .....	24
2.12	FD observation during November 4th - 13th, 2001. [Data provided by J. W. Bieber, 2003.] .....	26
3.1	The configuration for our simulations. ....	30
3.2	GCR intensity versus time in the year 2001. [Data provided by J. W. Bieber, 2003.] .....	32
3.3	GCR intensity ( $j$ ) versus time during DOY 238 to 251 in the year 2001. [Data provided by J. W. Bieber, 2003.] .....	34
4.1	Representative power spectrum of interplanetary magnetic turbulence, showing typical resonant wavenumbers for neutron monitor energies (“n”) and for muon detector energies (“ $\mu$ ”). The neutron monitor resonance is almost exactly at the turbulence correlation scale, $k = \lambda_c^{-1} \approx 3 \times 10^{-10} \text{ m}^{-1}$ . The model spectrum is from equation (13) of Bieber et al. (1994). ....	40
4.2	Intensity distribution, $j$ , of Galactic cosmic rays as a function of $\mu$ and $z$ (in units of $\lambda$ ) near an oblique shock with $\theta_{Bn} = 76^\circ$ for (a) $q = 0.5$ and (b) $q = 1.0$ . ....	46
4.3	Simulated Galactic cosmic ray intensity as a function of $\mu$ near an oblique interplanetary shock at $z = 0.025\lambda$ (solid line), $z = 0.125\lambda$ (dashed line), and $z = 1.575\lambda$ (dotted line) for $\theta_{Bn} = 76^\circ$ and $q = 1$ . ....	47
4.4	(a) Loss cone decay length, $\ell$ (in units of $\lambda$ ), as a function of $q$ for shock-field angles $\theta_{Bn} = 5.7^\circ$ (●—●), $14.0^\circ$ (◇⋯◇), $26.6^\circ$ (‡—‡), $45.0^\circ$ (×⋯×), and $76.0^\circ$ (★—★). (b) The quantity $\ell \cos \theta_{Bn} / \lambda$ ,	

	which determines precursor lead time in the case of radial shock propagation, as a function of $q$ for the same shock-field angles.....	51
4.5	Loss cone opening angle, $\theta_{HW}$ , as a function of the shock-field angle $\theta_{Bn}$ for $q = 0.1$ ( $\bullet\text{---}\bullet$ ), $0.5$ ( $\# \cdots \#$ ), $1.0$ ( $\diamond\text{---}\diamond$ ), and $1.5$ ( $\times \cdots \times$ ).....	52
5.1	The configuration for our Forbush decrease simulation.....	61
5.2	The simulation results of Forbush decrease.....	71
5.3	Observation of a Forbush decrease during DOY 239 to 240 in the year 2001. [Data provided by J. W. Bieber, 2003.].....	72



สถาบันวิทยบริการ  
จุฬาลงกรณ์มหาวิทยาลัย

# List of Tables

Table	Page
4.1 Angular Width and Decay Length of Loss Cone Features . . . . .	50
4.2 Estimated Loss Cone Lead Times . . . . .	55



สถาบันวิทยบริการ  
จุฬาลงกรณ์มหาวิทยาลัย

# Chapter 1

## Introduction

Humans have always wondered about space outside the Earth and have been continuously trying to study it. When the technology for travelling outside the Earth was not available, scientists studied what came from space, i.e., meteorites, light from objects in the sky, and aurorae. The term “cosmic rays” was first introduced after an Austrian physicist, Victor Hess, presented the results from his balloon flight and electroscopes to confirm that there were radiations coming from outside the Earth. A great deal of experiments and research have been actively conducted since then. It was later discovered that cosmic rays are not only electromagnetic radiation but also particles, e.g., electrons, protons, and other ions. Then, questions about where they come from and how they travel to our Earth arose. It has now been firmly established that cosmic rays can come from two types of sources: inside the heliosphere, e.g., from the Sun, and outside the heliosphere [Friedlander, 1989].

The cosmic rays originating from the Sun are now known as Solar Energetic Particles (SEPs). Those that originated from outside the Solar System are galactic cosmic rays (GCRs), which come from our galaxy, and extra-galactic

cosmic rays (EGCRs), which come from outside our galaxy. We could distinguish each type from the others by their energy. The further they are from, the higher energy they have. This is discussed in more detail in Chapter 2.

Since most cosmic ray particles are charged, their motion from one place to another is dominated by magnetic fields, which are present almost everywhere in space. There are many mechanisms and processes involved in the particle transport, for example, streaming, convection, deceleration, diffusion and drifts, which are not yet completely understood.

This work is an attempt to understand the nature of the particle transport, particularly in the region between the Sun and the Earth and near the Earth when there is solar activity. The situation studied in this thesis is the well known “Forbush Decrease” phenomenon.

A “Forbush decrease” means

*A temporary decrease in the number of galactic cosmic rays reaching the Earth; also known as Forbush Effect*

as written in the Oxford Dictionary of Astronomy [Ridpath, 1997]. In fact, the term is also used to refer to a temporary decrease in the intensity of galactic cosmic rays observed anywhere in the heliosphere and has an asymmetrical pattern of a sudden decrease over a few hours and an almost exponential recovery over a few days [le Roux & Potgieter, 1991]. A Forbush decrease might be considered a short-term, non-recurrent cosmic ray variation.

The well-known classical 2-step Forbush decrease is a result of the activity at the Sun. When the Sun explodes, it sometimes releases a large amount of mass with high velocity known as a coronal mass ejection (CME). Because of the difference in velocity between the CME and the solar wind, a discontinuity known

as a shock is formed in front of the CME. As the CME and its shock move toward the Earth, they sweep out the galactic cosmic rays which are usually uniformly detected by the world-wide neutron monitor network at ground level. The first step of the Forbush decrease results as the sheath region between the shock and the CME passes the Earth. If the CME itself passes the Earth, it causes the second step decrease.

Apart from understanding physical processes of particle transport, the study of Forbush decreases can help to predict space weather effects at the Earth. According to observations, there are precursory decreases known as “loss cone” effects before the shock arrives at Earth and causes severe damage to human activities.

Although Forbush decreases were first explained in 1937 by Scott Ellsworth Forbush (1904-1984) when so little was known about particles from outside the Earth, no complete explanation has yet been provided. One of the reasons why progress has been slow, despite the availability of methods of analyzing the cosmic ray data, has been the inability, until recently, to clearly distinguish the two components of Forbush decreases and their relationship with solar wind structures [Cane, 2000].

This work studies the first step of Forbush decreases by modelling and performing detailed time-dependent of numerical simulations of GCRs in the vicinity of an interplanetary shock. The model takes into account the particle pitch angle. This provides information on the GCR anisotropy, which is not fully understood yet. In order to understand the GCR observations at Earth relative to GCR in space, the Compton-Getting anisotropy has been studied also.

In Chapter 2, we present background knowledge which is essential to this

work. Chapter 3 contains an analysis on Compton-Getting anisotropies performed on GCR counts measured by neutron monitors on Earth to obtain an understanding of GCR anisotropy in the solar wind frame of reference when Forbush decrease occurs. A model of the loss cone precursor and its plausible application to advance prediction of space weather is discussed in Chapter 4. The simulations of Forbush decreases are finally explained and analyzed in Chapter 5.



สถาบันวิทยบริการ  
จุฬาลงกรณ์มหาวิทยาลัย



# Chapter 2

## Theoretical Background

This chapter will give an overview of the background knowledge that is essential to this work. A Forbush decrease is a heliospheric phenomenon, so it is necessary to consider constituents in the region where it takes place and what processes are responsible. These include the solar wind, interplanetary magnetic fields, coronal mass ejections, cosmic rays, and interplanetary shocks.

### 2.1 Solar Wind and Interplanetary Magnetic Fields

The solar wind is a fully ionized plasma radially expanding from the Sun's corona to the boundary of the heliosphere, called the heliopause, where the solar plasma pressure is balanced by the pressure of interstellar material [Kirk et al., 1994; Parks, 1991; Cravens, 1997; Russell, 2001; Burlaga, 1995]. Parker demonstrated that the Sun's corona is not in static equilibrium, which leads to an imbalance between the pressure gradient and the gravitational force causing the wind to be accelerated to supersonic velocities [Parker, 1963]. The speed of the solar wind is on average 400 km/s at the heliospheric equatorial plane and up to 800

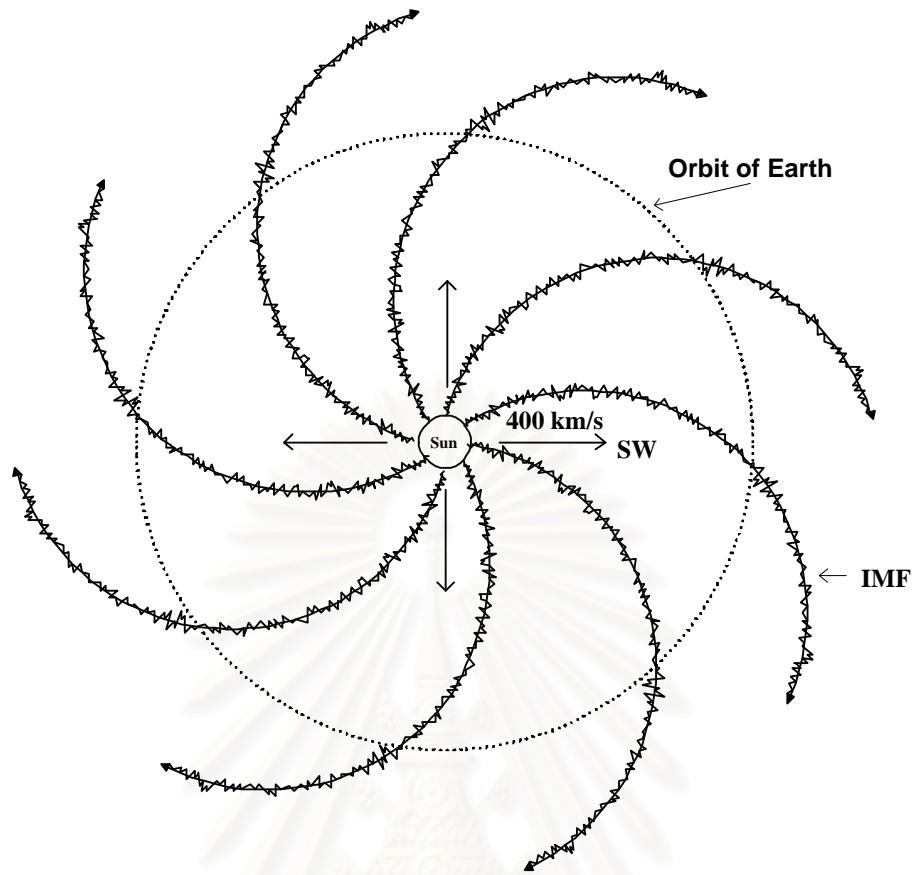


Figure 2.1: Archimedean spiral interplanetary magnetic field lines in the heliospheric equatorial plane (not to scale).

km/s (during “solar minimum” conditions) near the poles. Therefore, the Sun releases about 1 million tons of matter out into space every second. The solar wind consists mainly of elementary particles such as protons (90%), electrons, other ions, and plenty of neutrinos [Parks, 1991]. The density of the wind is approximately 5 particles/cm<sup>3</sup> at the temperature of 150,000 K at the distance of 1 AU near the Earth. Since the solar wind is tenuous, the particles rarely experience collisions. Its speed hardly decreases while travelling to the solar wind termination shock.

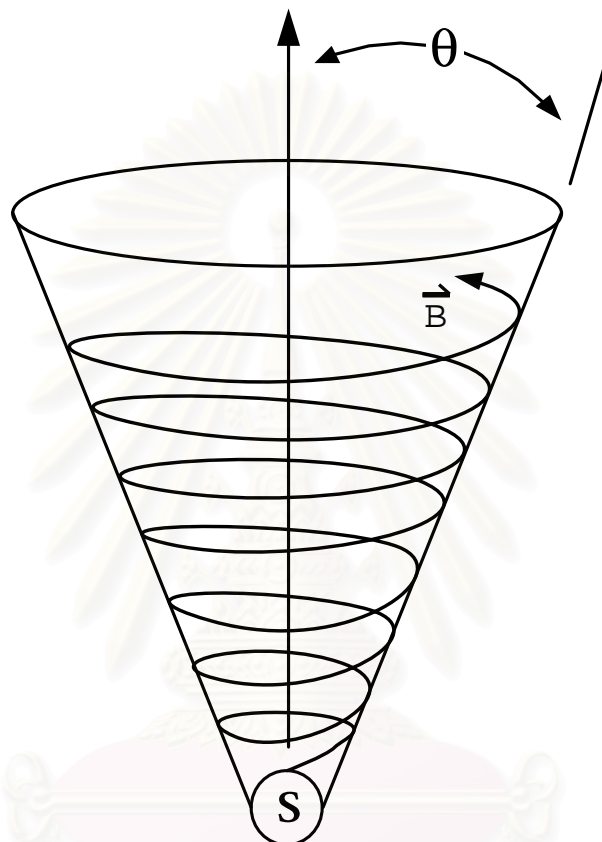


Figure 2.2: A sketch of an interplanetary magnetic field line for higher heliospheric latitudes (not to scale). The magnetic field line wraps around a cone whose surface has an angle  $\theta$  with respect to the rotation axis.

สถาบันวิทยบริการ  
จุฬาลงกรณ์มหาวิทยาลัย

The Sun has a strong magnetic field which tends to be carried outward by the solar wind because the solar wind is a highly electrically conducting plasma in which the field is “frozen in.” Since the Sun rotates about its axis, the plasma flow drags the magnetic field out into space with a shape of spiral with respect to a fixed point on the Sun. The solar rotation speed at a given latitude is constant in time, as is the solar wind speed from a given location on short time scales, so the interplanetary magnetic field has a pattern of an Archimedean spiral in the ecliptic plane, or at general latitudes, it spirals on the surface of a cone centered on the rotational axis. The source of the solar wind acceleration is uncertain and the process generating it is not quite understood. The fluctuation in the solar wind flow causes the irregularity in the interplanetary magnetic field (IMF). The IMF has a magnitude of 5 nT on average near the ecliptic plane, but is highly variable elsewhere. Figure 2.1 illustrates the 400 km/s solar wind incorporated with the spiral interplanetary magnetic field in the heliospheric equatorial plane. The spiral IMF on the surface of a cone around the solar polar axis is shown in Figure 2.2.

Similarly to a bar magnet, the Sun’s magnetic field is roughly dipolar. The magnetic field lines emerge from one hemisphere and return to the other hemisphere after a long intricate journey with the solar wind. The transition region between toward-fields (negative magnetic polarity) and away-fields (positive magnetic polarity) in the interplanetary medium is called the magnetic neutral sheet or the heliospheric current sheet (HCS). The polarities usually switch every 22 years, also known as the solar magnetic cycle. Figure 2.3 displays a two-dimensional side view of magnetic field lines resulting from a coronal expansion model with a dipolar surface field, where the dotted curve indicates the HCS. A



Figure 2.3: The two-dimensional side view of the HCS.

drawing of a three-dimensional side view of a warped HCS is shown in Figure 2.4.

Both the solar wind and the IMF play important roles in most astrophysical processes in the heliosphere, particularly particle transport. All kinds of events inevitably take into account the solar wind as a significant component. The solar wind is responsible for auroral lights, fuelling magnetospheric storms, and forming a planet's magnetosphere.

They are definitely significant effects for Forbush decreases. This work applies the solar wind speed and IMF parameters obtained from the magnetohydrodynamic (MHD) simulation of a generic coronal mass ejection performed by Dr. David Lario.

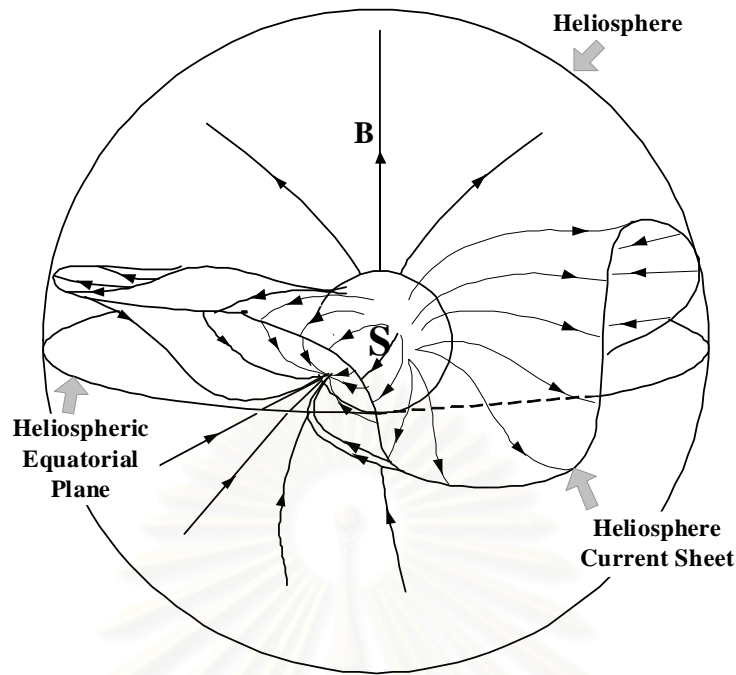


Figure 2.4: A schematic drawing of the heliospheric current sheet (HCS).

## 2.2 Coronal Mass Ejections (CMEs)

Coronal mass ejections are large scale explosions in the Sun's corona that spew out solar plasma along with various configurations of solar magnetic field lines [Cravens, 1997]. Figure 2.5 shows a photograph of an actual CME as it just lifted off the Sun. It is believed that a mechanism of the ejection is magnetic reconnection at the Sun. However, what drives the reconnection is still confusing. CMEs are often associated with solar flares, or disappearing filaments in quiet regions (in other words, eruptive prominences seen on the disk of the Sun) [Schwenn, 1983; Hundhausen, 1988; Gosling et al., 1990]. Sometimes, a CME was seen before a flare or a disappearing filament. Indeed, for low-speed CMEs there is little correlation between flare times and CME times [Zhang et al., 2002]. This suggests that the flares and the disappearing filaments do not actually drive the

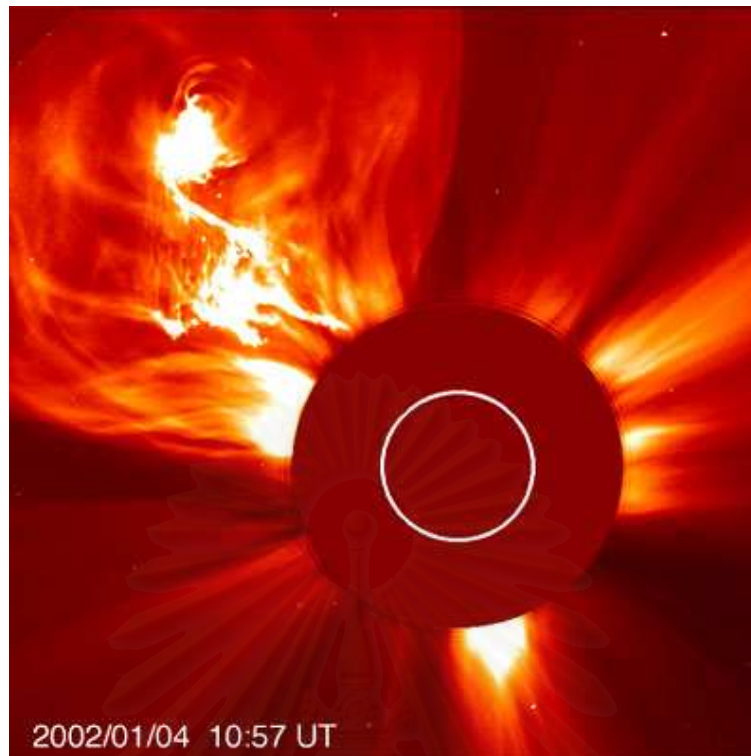


Figure 2.5: A photograph of a CME taken by the SOHO spacecraft. [Taken from <http://sohowww.nascom.gov>]

magnetic reconnection to generate a low-speed CME. The cause of CMEs is still mysterious.

The literature on CMEs is vast and poorly organized with numerous conflicting ideas and imaginative extrapolations based on very incomplete observations. Some CMEs have magnetic fields that are highly ordered and connected to the Sun, while others have disordered magnetic fields and are disconnected from the Sun [Burlaga, 1995]. Figure 2.6 is a plausible drawing of a CME associated with the powerful solar event that occurred on July 14, 2000. From observations, this CME could be viewed as a large-scale magnetic flux rope expanding in interplanetary space [Ihara et al., 2001]. The ejecta are not a part of the ambient solar wind and, therefore, are magnetically disconnected from it.



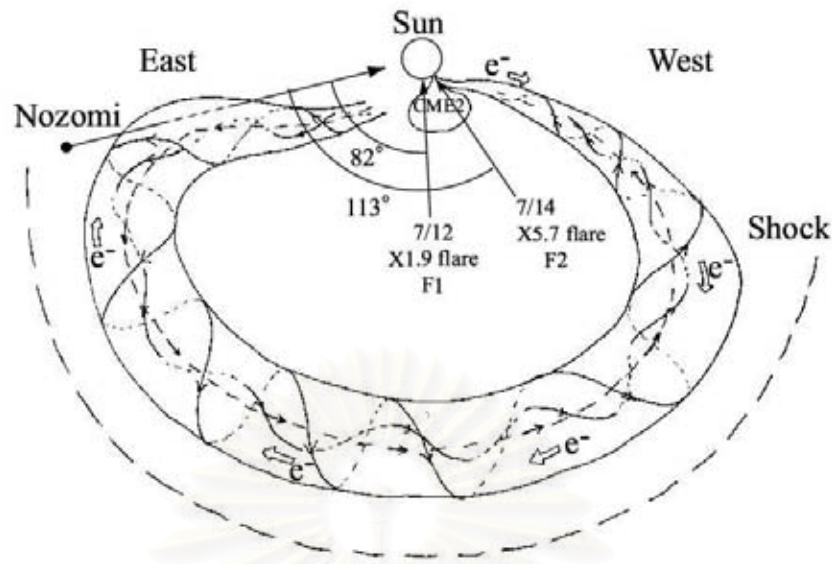


Figure 2.6: A plausible drawing of a CME [Ihara et al., 2001].

A CME can comprise  $10^{15}$  -  $10^{16}$  grams of coronal material and can propagate into space with a wide range of speeds, say, from  $300 \text{ km/s}^{-1}$  to  $2000 \text{ km/s}^{-1}$  [Zhang et al., 2002]. It can seriously disrupt the near-Earth space environment. Intense radiation from the Sun, which arrives only 8 minutes after being released, can alter the Earth's outer atmosphere, disrupting long-distance radio communications. Energetic particles accelerated by the shock wave driven by a CME can endanger astronauts or damage satellite electronics. These energetic particles arrive at the Earth about an hour later after reaching the ACE spacecraft at the inner Sun-Earth Lagrangian point (L1). The actual CME arrives at the Earth one to four days after the initial eruption, possibly resulting in strong geomagnetic storms, aurorae and electrical power blackouts.

At present, there is no single theoretical model that applies to all CMEs. A CME is new, fresh magnetic plasma from the Sun with few particles from other



sources, such as Galactic cosmic rays. The region inside a CME is believed to be responsible for the second step of Forbush decreases (to be discussed in Chapter 3). As mentioned in the introductory chapter, this work studies the first step of Forbush decreases corresponding to the region in front of a CME. In other words, it is the region just in front of a shock in the sheath between the CME and its shock. Dr. Lario kindly simulated a generic CME that drove an interplanetary shock for this work using a model based on Vandas et al. (1995).

## 2.3 Cosmic Rays and Their Transport in the Heliosphere

Cosmic rays are charged particles of high energy, which could be considered as a tool to study processes in interplanetary space. Their classification is based on their origin. The further they come from, the more processes they encounter. Solar Energetic Particles (SEPs) are cosmic rays that originate from the Sun. It is commonly known that they are accelerated to energies of about 0.1 - 10 MeV/amu (or occasionally up to 50 GeV) in association with transient explosive events at the Sun's surface such as flares or CMEs [Schlickeiser, 2002]. The relative elemental abundances of SEP vary strongly from one event to the next. Galactic Cosmic Rays (GCRs) are mostly protons that come from various sources outside the heliosphere but within the Milky Way galaxy and are distributed nearly isotropically in our solar system. The range of their energies is from tens of MeV to  $10^{19}$  eV. Extragalactic Cosmic Rays (EGCRs) come from sources outside our galaxy that somehow make their way to the heliosphere. Along their way, they underwent through many astrophysical processes that accelerated them to energies of up to  $3 \times 10^{20}$  eV.

We usually observe cosmic rays by using detectors on satellites, e.g., ACE and Ulysses, and on the Earth's surface, e.g., the neutron monitor network and muon detector network. Particle detectors on satellites can measure lower energy cosmic rays while those on the ground can measure only high energy cosmic rays that penetrate the Earth's magnetosphere. In order to completely understand cosmic ray observations, particle transport becomes an important issue.

A Forbush decrease is a temporal decrease in GCR intensity. This work therefore concentrates on processes responsible for the transport of GCRs, especially in the Sun-Earth region. Basic processes experienced by GCRs are convection, streaming, drifts, scattering, and focusing. Convection is an effect of the moving solar wind plasma. GCRs themselves have kinetic energy that results in streaming motions. Drifts are effects of large-scale perpendicular gradients or curvature in magnetic fields on the cosmic ray motion. Scattering is caused by interplanetary magnetic field irregularities, and focusing is caused by divergence or convergence of the magnetic fields.

## 2.4 Interplanetary Shocks

As a fast CME propagates radially out into the solar wind, the ambient field lines are pushed aside and get wrapped around the western edge of the ejecta. When CMEs travel with a high speed, a shock develops, and extends beyond the angular extent of the ejecta [Cane, 1995] as shown in Figure 2.7. It could be said that a shock is a discontinuity in solar wind parameters, i.e., the solar wind speed, the interplanetary magnetic fields, and the solar wind density. Between a CME and its shock there is a region of compressed and turbulent magnetic fields. Therefore, CMEs and their shocks have significant effects on the GCR transport.

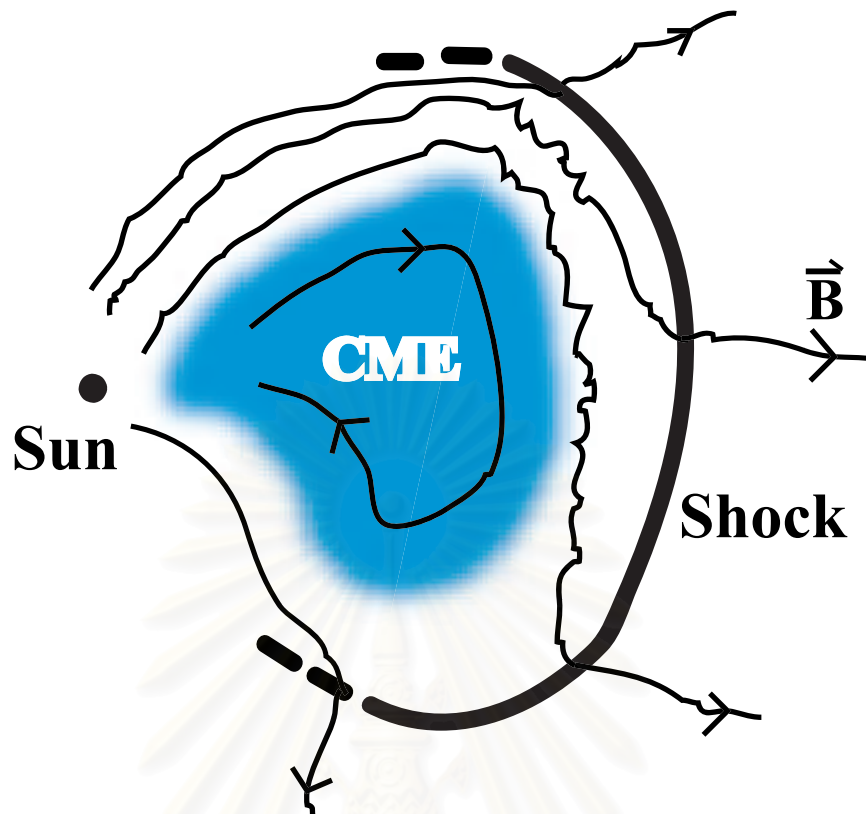


Figure 2.7: An illustration of a CME, its driven shock, and interplanetary magnetic fields.

Interplanetary shocks are well-known for accelerating particles to high energies. In the case of a Forbush decrease, the shock manifests itself as an obstruction that reflects GCRs causing a decrease in the first step of Forbush decreases and their precursors. Various space weather effects result when a shock compresses Earth's magnetic fields causing geomagnetic storms.

Interplanetary shock properties and how these properties change with distance from the Sun strongly depend on the characteristics of their driving CMEs, e.g., their speeds and locations on the Sun. Particle signatures from a shock depend on 1) the size and speed of the shock, 2) the evolution of the shock and 3) the location of the observer. For shocks going fast enough to accelerate

particles, observers who intercept the associated ejecta see the highest intensities. Those observers for which the ejecta passes to their west see little or no effect of the shock. In contrast if the ejecta pass to the east of an observer, a long-lived enhancement is observed after the shock has passed.

## 2.5 Cosmic Ray Observations during Forbush Decreases

Forbush decreases are probable consequences of CMEs and their driven shocks as explained in Chapter 1. Figure 2.8 schematically shows GCR counts when a FD takes place. Consider a detector measuring GCRs as a function of time in the pathway of the CME and its shock. At early times, the detector is in the region where the shock has not yet arrived, called the upstream region. At later times, the detector is in the region where the shock has already passed, called the downstream region. This is schematically indicated in Figure 2.8: with increasing time, the detector effectively surveys along a line through the shock/CME structure, from right to left. As shown, the first step of a Forbush decrease occurs when the detector is in the sheath region between the CME and its shock. A second step decrease occurs if the CME ejecta encounter the detector.

The GCR counts or signatures of Forbush decreases depend on various parameters, e.g., the properties of the CME and its shock, the type of detector, and the detector position with respect to the CME origin at the Sun [Lockwood, 1971; Wibberenz et al., 1997; Wibberenz et al., 1998; Cane, 2000]. This section surveys some current knowledge on the properties and the signatures of Forbush decreases according to observations.

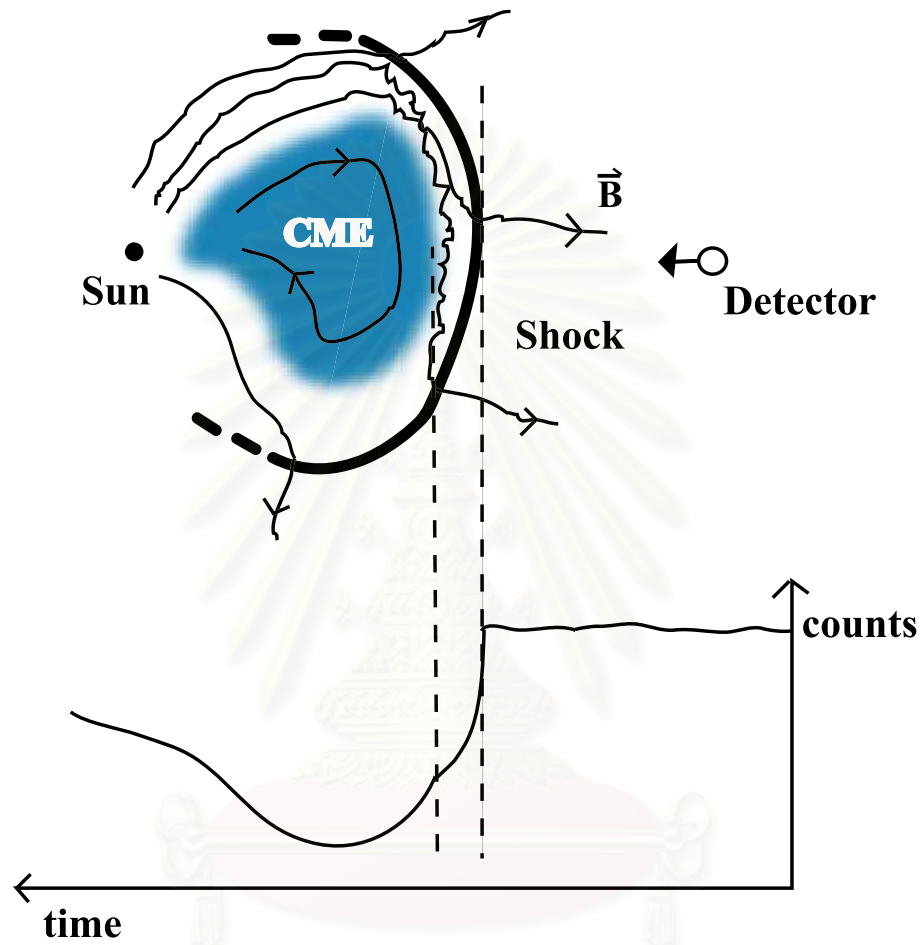


Figure 2.8: Schematic of GCR counts as a function of time as a CME and its shock pass by a detector.

สถาบันวิทยบริการ  
จุฬาลงกรณ์มหาวิทยาลัย

### 2.5.1 General Observations in Space and on Earth

Observations of Forbush decreases in space are made by particle detectors on spacecraft, while those on the Earth are obtained from neutron monitors and muon detectors. The Earth effectively serves as a detector at a certain location in space that detects cosmic rays (mostly GCR) with sufficient energy to pass through the Earth's magnetic field. Particle detectors on spacecraft measure lower energy particles at various locations as they travel through space. For different energies, the Forbush decreases are different for the same solar event. The position in space also has an important effect on the shape of the decrease.

The characteristics of each step of FD significantly depend on the motion of the shock and CME past the detector, as shown in Figure 2.9. Both steps are distinctively seen for passage A as the detector encountered both the shock and its associated CME. Passage B represents an observation made by a detector that only encounters the shock but not the CME. This can occur because shocks have a greater longitudinal extent than their associated CMEs [Cane, 2000].

As seen in Figure 2.9, in observations of cosmic ray count rates it is not always clear whether shocks or CMEs have passed the detector. Solar wind data obtained from other instruments on spacecraft could help indicate times of shock and CME arrivals. From Figure 2.10, it is clear that when the shock arrives, there are sudden changes (at the vertical solid line) in the magnetic field magnitude and its component out of the ecliptic plane, and the proton temperature, density and speed. The horizontal dashed line in the temperature panel (panel 3 from the top) shows the expected temperature for normal solar wind expansion. The blackened area is a low temperature region, indicative of CME material. The horizontal solid lines in the density panel (panel 4 from the top) indicate the



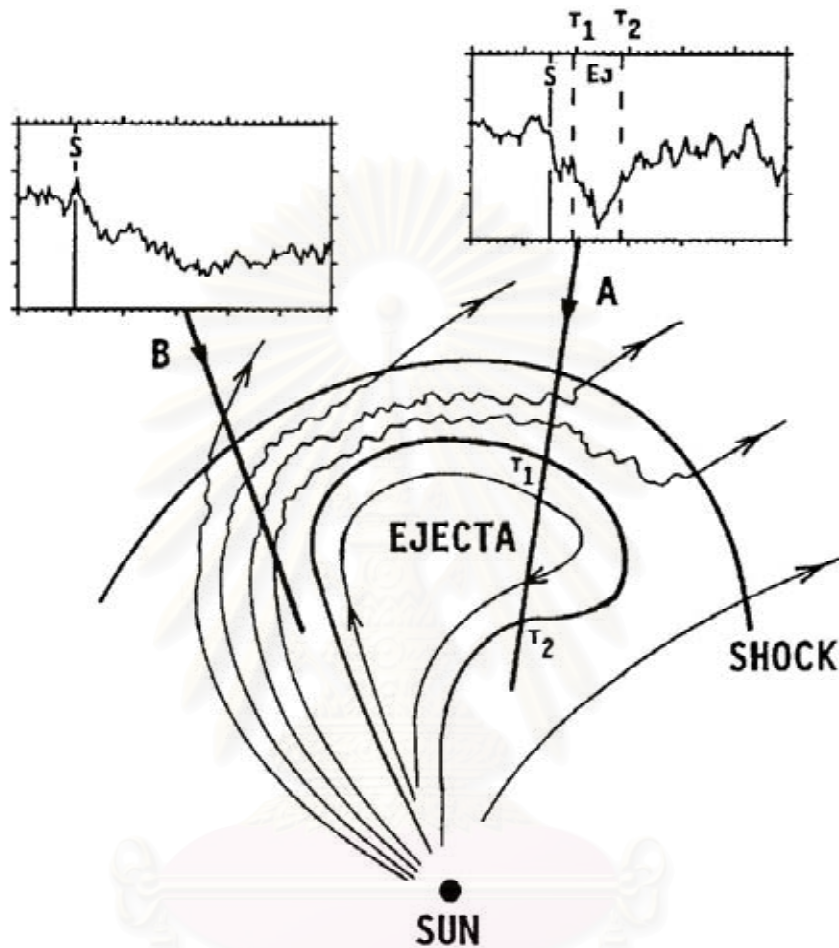


Figure 2.9: An illustration of Forbush decreases at two detector locations, A and B. Both detectors observe a first-step FD at the time of shock passage (S). At location A, both the shock and the CME pass the detector. The GCR flux is especially depressed when the ejecta pass by (for  $T_1 < T < T_2$ ) [Cane, 2000].

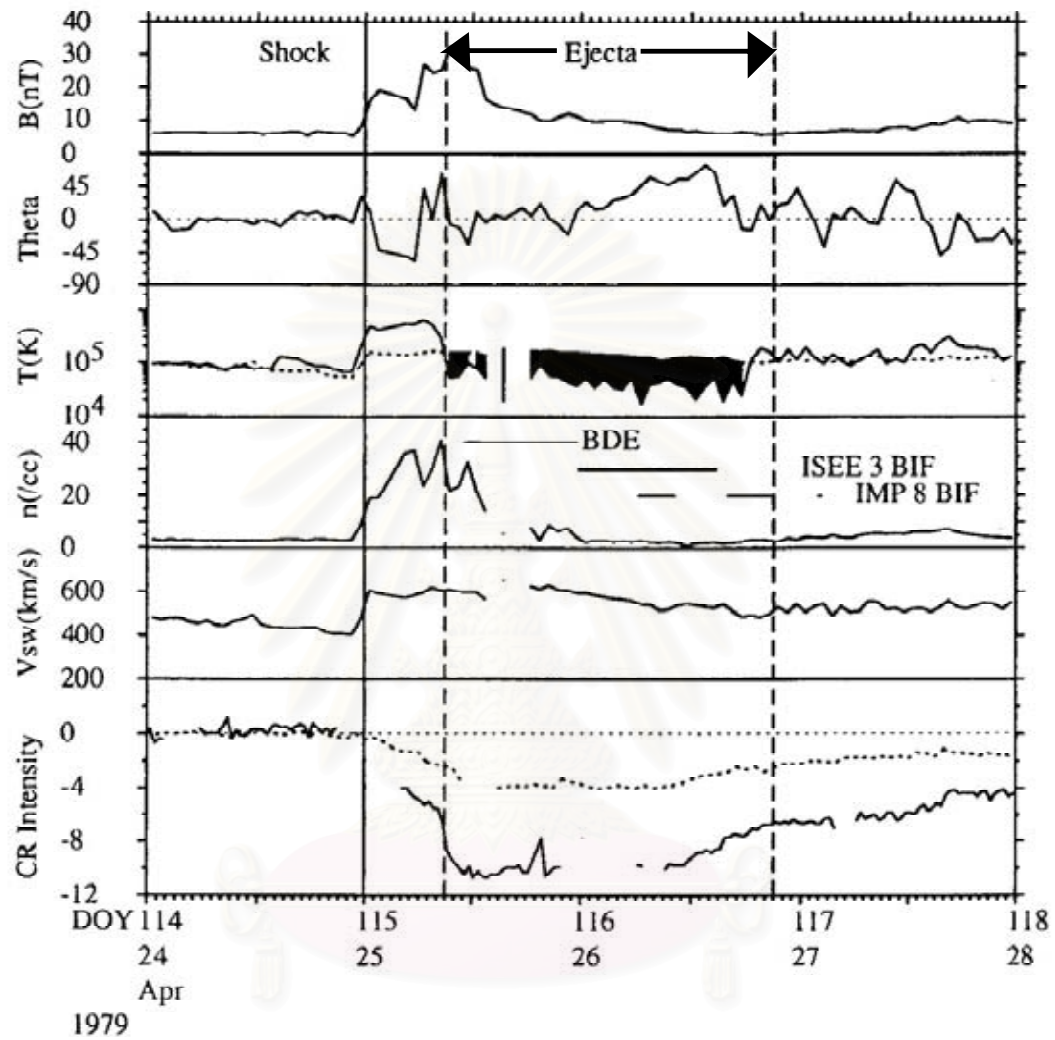


Figure 2.10: Various solar wind data as indicators for shocks and CMEs [Gosling et al., 1995].



durations of bidirectional solar wind electron heat flux (BDE) [Gosling et al., 1987] and  $\sim 1$  MeV bidirectional ion flows (BIF) measured by ISEE-3 and IMP 8 [Richardson & Reames, 1993]. Since bidirectional flows usually indicate closed field lines, the cessation of bidirectional electrons often seen inside ejecta has been interpreted by Gosling et al. (1995) as an indication of the presence of open field lines within CMEs that have reconnected with the ambient IMF.

At Earth, shock arrivals and resulting magnetic storms would be denoted by the Kp index and  $D_{ST}$  index. Kp is intended to be a “qualitative” measure of the planetary magnetic disturbance level, ranging from 0 to 9 with plus and minus designations. Higher Kp values imply more intense magnetic disturbance levels. The  $D_{ST}$  index provides information on magnetic storms and is constructed from world-wide mid-latitude and equatorial magnetograms. The  $D_{ST}$  is a negative value in units of nT and a more negative  $D_{ST}$  implies a more intense storm [Parks, 1991]. These would help in identifying a shock passage.

### 2.5.2 Magnitude

A large FD can have a magnitude in the range of a 10-25 % decrease in GCR measured by neutron monitors. CME characteristics have the most important effects on the magnitudes of FDs. Faster CMEs can generate more energetic shocks that sweep out more GCRs, and hence yield larger magnitude decreases. The magnitude of a FD also depends on the position of the observer. For the same event, a FD is believed to be larger in the inner heliosphere and smaller as the CME expands and is filled in by GCRs while propagating out to the outer heliosphere. The heliologitude and heliolatitude of the observer with respect to the CME origin (direction) and solar magnetic fields are also important determinants of the magnitudes of the decreases. At the same distance from the Sun, the

observer who is magnetically connected to the CME origin will experience more decrease than those who are not.

### 2.5.3 Rigidity Dependence

Most cosmic ray particles are charged. They are transported in the heliosphere by gyrating around interplanetary magnetic field lines. In a uniform static magnetic field  $\vec{B}$  the equation of motion for a charged particle of rest mass  $m_0$ , charge  $Ze$  and velocity  $\vec{v}$  is

$$\frac{d}{dt}(\gamma m_0 \vec{v}) = Ze(\vec{v} \times \vec{B}), \quad (2.1)$$

where  $\gamma = (1 - v^2/c^2)^{-1/2}$  is the Lorentz factor and  $c$  is the speed of light. The left hand side of the equation can be expanded as

$$m_0 \frac{d}{dt}(\gamma \vec{v}) = m_0 \gamma \frac{d\vec{v}}{dt} + m_0 \gamma^3 \vec{v} \frac{\vec{v} \cdot \vec{a}}{c^2}. \quad (2.2)$$

The acceleration  $\vec{a} = d\vec{v}/dt$  is always perpendicular to  $\vec{v}$  in the magnetic field and then  $\vec{a} \cdot \vec{v} = 0$ . Then Equation 2.1 becomes

$$\gamma m_0 \frac{d\vec{v}}{dt} = Ze(\vec{v} \times \vec{B}). \quad (2.3)$$

Now  $\vec{v}$  can be split into components parallel and perpendicular to the magnetic field. Equation 2.3 becomes,

$$\gamma m_0 \frac{d\vec{v}}{dt} = Ze v_{\perp} B (\hat{i}_v \times \hat{i}_B), \quad (2.4)$$

where  $\hat{i}_v$  and  $\hat{i}_B$  are unit vectors in the directions of  $\vec{v}$  and  $\vec{B}$  respectively. Considering centrifugal acceleration, it is found that

$$\frac{v_{\perp}^2}{r} = \frac{ZevB \sin \theta}{\gamma m_0}, \quad (2.5)$$

where  $r$  is the radius of gyration (gyroradius), the pitch angle,  $\theta$ , is the angle between  $\vec{v}$  and  $\vec{B}$ , and  $v_{\perp} = v \sin \theta$ . Equation 2.5 can be rearranged to read

$$r = \frac{\gamma m_0 v \sin \theta}{Ze} \frac{1}{B} = \left( \frac{pc}{Ze} \right) \frac{\sin \theta}{Bc}, \quad (2.6)$$

where  $p$  is the relativistic three-momentum of the particle. This means that particles with the same value of  $pc/Ze$  and pitch angle would follow exactly the same path in a static magnetic field. The quantity  $pc/Ze$  is called “rigidity” or “magnetic rigidity” of the particle. The rigidity can be expressed in units of gigavolts (GV).

Measuring cosmic rays on Earth, the magnetosphere, like a giant magnetic spectrometer, makes each NM station respond to a different minimum rigidity known as the “cutoff rigidity.” NMs can detect cosmic rays that have a rigidity exceeding the cutoff rigidity. At the Earth’s magnetic poles, the motion of incoming cosmic rays is mostly parallel to the geomagnetic field as shown in Figure 2.11. This allows particles even with low rigidity to reach NMs near the poles. It could be said that polar NMs have a low cutoff rigidity. On the other hand, NMs near the equator have a higher cutoff rigidity because the motion of cosmic rays is mostly perpendicular to the geomagnetic field. Cosmic rays need to have high rigidity to cross the geomagnetic field and reach the NMs. The latest planned Princess Sirindhorn Neutron Monitor station to be sited at Doi Inthanon, Thailand will respond to the world’s highest cutoff rigidity of 17 GV, and will therefore provide unique scientific data.

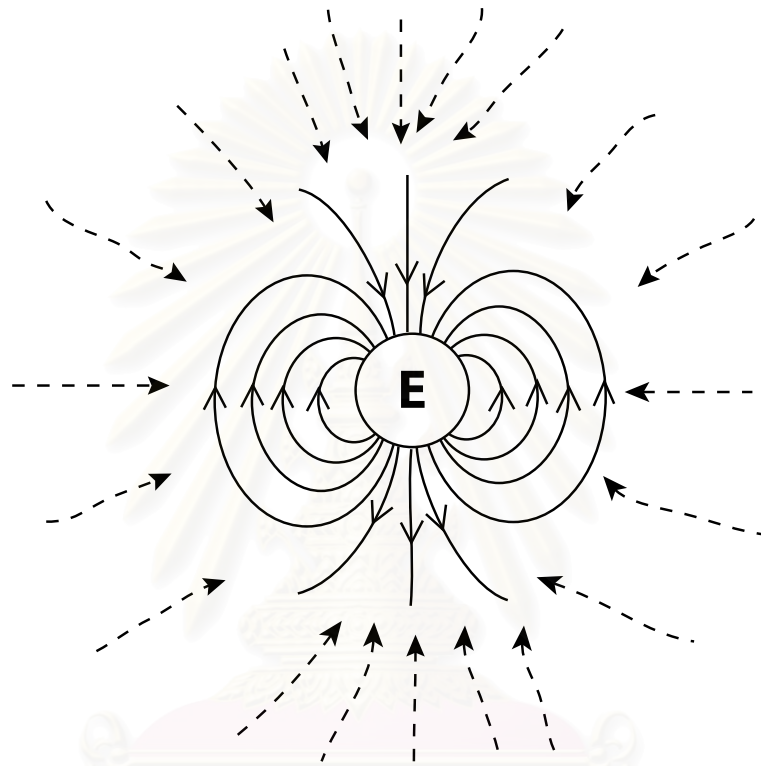


Figure 2.11: A schematic drawing of cosmic rays travelling toward the Earth (dashed lines) in the presence of the geomagnetic field (solid lines).

สถาบันวิทยบริการ  
จุฬาลงกรณ์มหาวิทยาลัย

At lower rigidities, the magnitudes of FDs appear to be larger than those at higher rigidity. Observations are consistent with a model in which amplitudes of FDs are proportional to  $P^{-\gamma}$ , where  $P$  is the rigidity and  $\gamma$  has values of 0.4-1.2 [Cane, 2000]. There are difficulties in determining the rigidity dependence because of the large anisotropy and because the rigidity dependence varies rapidly during the decrease. It has been concluded that solar activity (depending on the 11-year solar cycle) and solar polarity (during the 22-year solar magnetic cycle) have no effects on the rigidity dependence [Kolomeets et al., 1965; Morishita et al., 1990].

#### 2.5.4 Anisotropy and Precursory Effects

The GCR distribution is nearly isotropic at Earth, i.e., GCRs arrive nearly uniformly from all directions. When there are disturbances, e.g., CMEs and shocks, they obstruct the GCR flow in certain directions and cause “anisotropy” during the FDs. In some cases, the cosmic ray distribution function could be described as

$$F(\hat{n}) = F_0(1 + \vec{\delta} \cdot \hat{n}), \quad (2.7)$$

where  $F(\hat{n})$  is the cosmic ray distribution function in a certain direction  $\hat{n}$ ,  $F_0$  is the omnidirectional cosmic ray distribution function, and  $\vec{\delta}$  is the cosmic ray anisotropy vector. [More generally,  $\vec{\delta}$  can be defined as the corresponding first order (vector) coefficients in a spherical harmonic expansion.]

Neutron monitors at different locations measure cosmic rays that come from different directions in space (called “asymptotic directions”). They provide us information on cosmic ray anisotropies during FDs. According to neutron monitor observations, there are sometimes increases and decreases in GCR in-

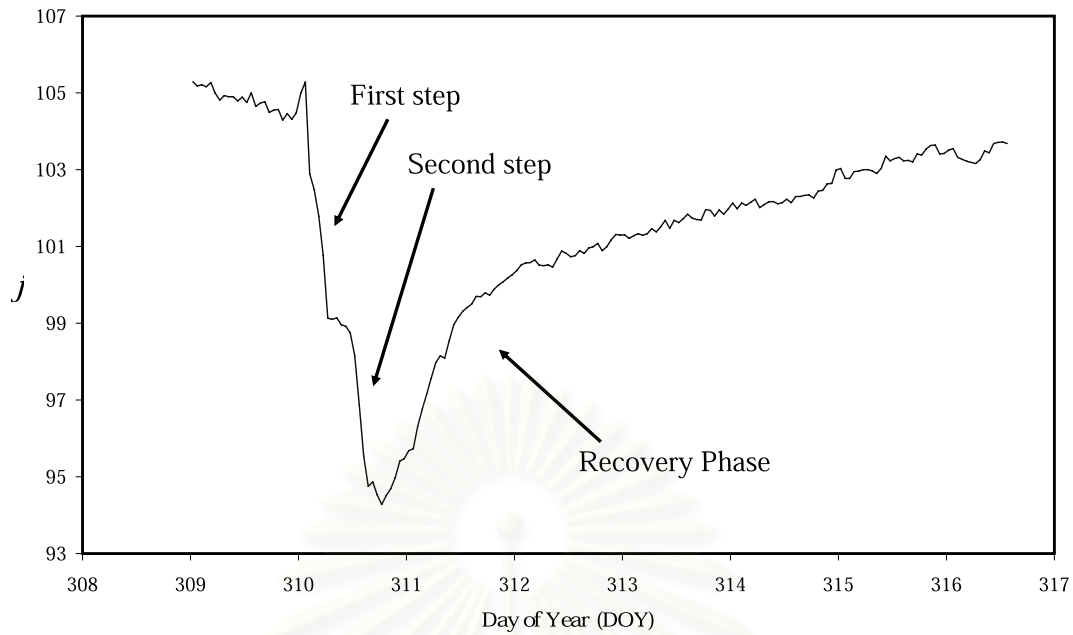


Figure 2.12: FD observation during November 4th - 13th, 2001. [Data provided by J. W. Bieber, 2003.]

tensity of some directions before the first step FDs appear, i.e., before the shock arrival. These are called precursory effects.

This work also concentrates on anisotropies caused by particle transport at shocks and in particular precursory increases and decreases. Precursory effects are generated by density gradient flows across the shocks. According to observations, precursory increases are seen less clearly than precursory decreases. Precursory decreases known as loss cone precursors can be used as a tool for advance warning of space weather effects [Ruffolo, 1999; Leerunnavarat et al., 2003].

### 2.5.5 Recovery Characteristics

After the first step and the second step of the decrease occur, there is a recovery phase in which the cosmic ray intensity rises to about the same level as before

the decrease. An example of an observed FD is shown in Figure 2.12. This event occurred during Day of Year (DOY) 308 - 317 of the year 2001 (November 4th to November 13th, 2001), which is measured by neutron monitors.

FDs can characteristically recover exponentially with a time constant of  $\sim 3 - 10$  days at Earth [Lockwood et al., 1986]. Like the magnitudes of FDs, recoveries depend on the position in the heliosphere with respect to the origin of solar activity [Barnden, 1973; Iucci et al., 1979; Cane et al., 1994]. As the radial distance increases, the recovery time for FDs is greater, being of the order of months in the outer heliosphere [Van Allen & Mihalov, 1990], while the magnitude becomes smaller. It is found that recovery times are independent of rigidity within the rigidity range of  $\sim 2 - 5$  GV, and are independent of solar polarity or time in the solar magnetic cycle [Lockwood et al., 1986].

Most FDs do not fully recover before the next FD occurs. Therefore, it has been proposed that long-term modulations, such as the 27-day cosmic ray modulation, are caused by the pile up many fast CMEs in so-called global merged interaction regions (GMIRs) located in the outer heliosphere. GMIRs are thought to be related to the merging of systems of transient flow, e.g., CMEs, with other streams. However, many recent works [Cliver et al., 1993; Cane et al., 1999a; Cane et al., 1999b] argued that the long term modulation is not well-correlated with fast energetic CMEs. They found that the modulation was not matched by an increase in the CME rate.



## Chapter 3

# Compton-Getting Anisotropies during Forbush Decreases

The Compton-Getting anisotropy is caused by the motion between an observer and a reference frame in which a particle flux is specified [Compton & Getting, 1935; Gleeson & Axford, 1968; Forman, 1970]. When particles move with very high speed with respect to an observer, their momenta appear differently in the observer frame of reference. The signatures of the difference, known as the Compton-Getting effect, depend on both the magnitude and direction of the particle's motion respective to the observer.

The equation of particle transport used in this work is defined in a mixed frame of reference where the particle momentum is in the solar wind frame, and the spatial distance and time are in the shock frame. The particle transport at the shock is calculated in the shock frame in which the de Hoffmann-Teller (dHT) frame is used. The dHT frame is the frame where the shock is stationary, the solar wind flow is parallel to the magnetic field, and the electric field is



zero [de Hoffmann & Teller, 1950]. Therefore, the solar wind frame and the de Hoffmann-Teller frame are moving respective to the frame where the GCR flux is observed. Figure 3.1 shows the configuration in which our simulations take place. The vertical dashed line represents a shock which is the discontinuity in solar wind parameters, e.g., the interplanetary magnetic field represented here by oblique solid lines. In this case, the shock is moving to the right. On the left side of the shock is the region called “downstream” where the shock has passed. Upstream of the shock is on the right side of the shock where the shock has not yet arrived. Point A is where the magnetic field lines cross the shock. The dHT frame is the frame in which point A is stationary. In order to clearly understand our results, a Compton-Getting anisotropy analysis is performed on observational data of cosmic rays to obtain the cosmic ray distribution function in the solar wind frame, which then be transformed to the de Hoffmann-Teller frame. The purpose of this exercise is to determine the significance of the Compton-Getting effects.

The Lorentz invariance states that the phase space density in all frames is the same as expressed in Equation 3.1.

$$f(\vec{p}) = f'(\vec{p}'), \quad (3.1)$$

where primed quantities refer to the moving solar wind frame and unprimed quantities refer to the Earth frame. The phase space density of cosmic rays could be described as a power law in momentum ( $f(p) \propto p^{-\gamma}$ ). For GCRs during FDs,  $\gamma$  is found to be 3.7 while it is 2.7 for isotropic cosmic rays. The Compton-Getting effect is simply a result of the difference in momentum in the two frames as shown in Equation 3.2. Note that the intensity is related to the phase space density by  $j = p^2 f$ .

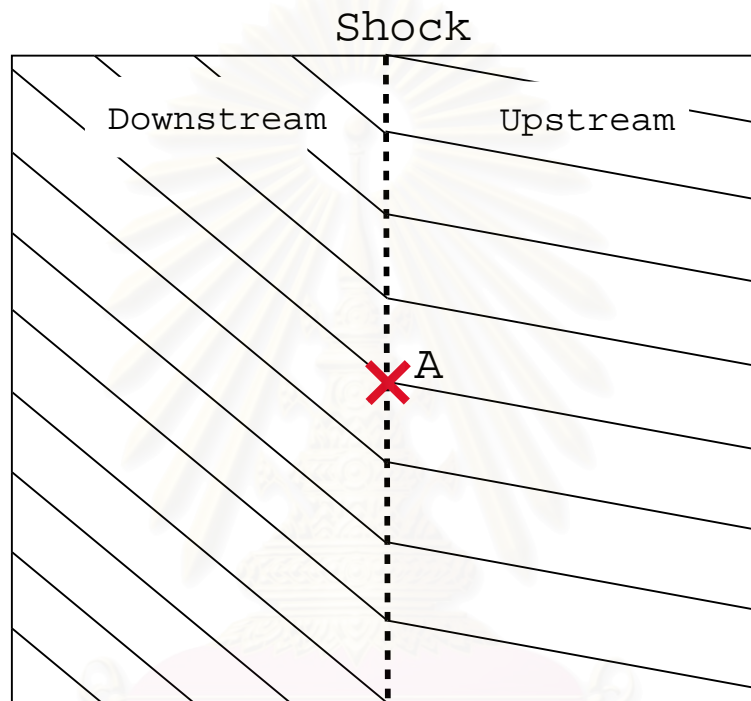


Figure 3.1: The configuration for our simulations.

สถาบันวิทยบริการ  
จุฬาลงกรณ์มหาวิทยาลัย

$$\begin{aligned}
\frac{j}{j'} &= \frac{p^{-\gamma}}{p'^{-\gamma}} \\
&= \frac{(p + dp)^{-\gamma}}{p^{-\gamma}} \\
&= \left(1 + \frac{dp}{p}\right)^{-\gamma} \\
&\approx \left(1 - \gamma \frac{dp}{p}\right), \tag{3.2}
\end{aligned}$$

where  $dp$  depends on the direction of the moving solar wind with respect to the fixed frame. For a certain direction  $\hat{n}$ , the Compton-Getting effect in Equation 3.2 would then be

$$\frac{j}{j'} = \left(1 + \gamma \frac{\hat{n} \cdot \vec{V}_{sw}}{v}\right), \tag{3.3}$$

where  $\vec{V}_{sw}$  is the velocity of the solar wind frame relative to the fixed frame and  $v$  is the particle velocity of interest.

For neutron monitors, anisotropy components can be derived from Equation 2.5 as follows:

$$j(\hat{n}) = j_0 + j_0(\vec{\delta} \cdot \hat{n}). \tag{3.4}$$

Each neutron monitor station measures cosmic rays at a certain direction in the sky. The cosmic ray intensity in the Earth fixed frame would then be written as

$$\begin{aligned}
\vec{j}(\hat{n}) &= n + \vec{\xi} \cdot \hat{n} \\
&= n + \xi_x n_x + \xi_y n_y + \xi_z n_z, \tag{3.5}
\end{aligned}$$

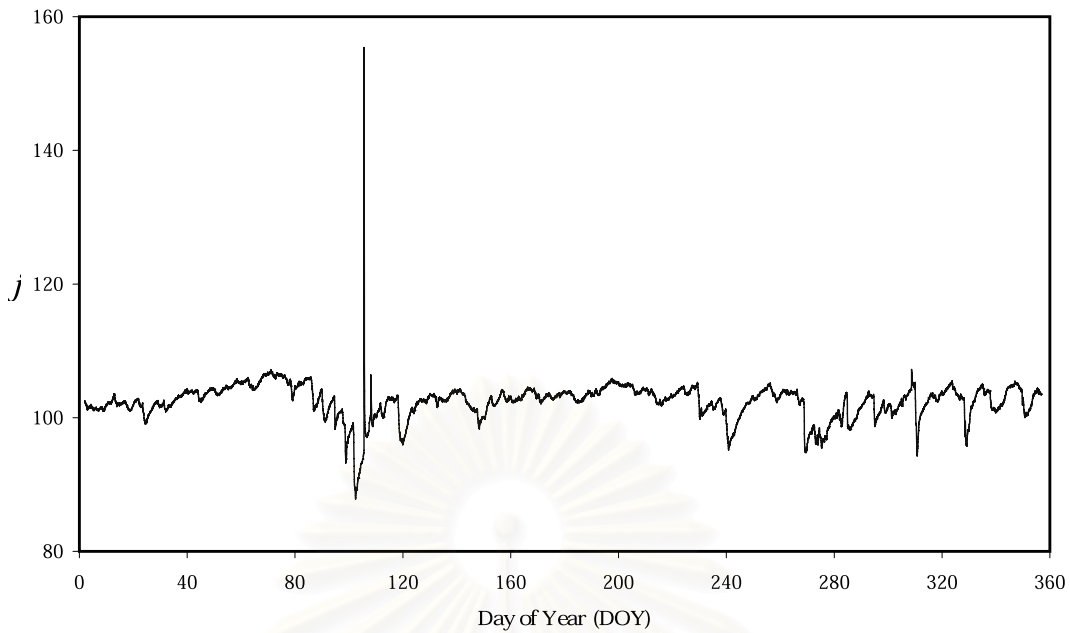


Figure 3.2: GCR intensity versus time in the year 2001. [Data provided by J. W. Bieber, 2003.]

where  $\hat{n}$  is the direction outward from a neutron monitor station,  $n$  is cosmic ray intensity averaged over all directions, and  $\xi_x$ ,  $\xi_y$ , and  $\xi_z$  are three components of anisotropy multiplied by the intensity.

The transformation of the observational data measured by a neutron monitor in the Earth frame to the moving solar wind frame can be done by incorporating Equation 3.3 into Equation 3.5 to yield

$$\begin{aligned}
 j'(\hat{n}) &= n + \left(\xi_x - n\gamma\frac{V_x}{v}\right)n_x + \left(\xi_y - n\gamma\frac{V_y}{v}\right)n_y + \left(\xi_z - n\gamma\frac{V_z}{v}\right)n_z \\
 &= n + \left(\vec{\xi} - \frac{n\gamma}{v}\vec{V}\right) \cdot \hat{n}.
 \end{aligned} \tag{3.6}$$

Note that the change in direction is negligible, i.e.,  $\hat{n} \approx \hat{n}'$ .

The de Hoffmann-Teller frame (the shock frame) is then moving with a speed of  $[(U_n \sec \theta)/c] \cdot \hat{B}$  with respect to the solar wind frame. Here  $U_n$  is the solar

wind speed in the direction normal to the shock plane,  $\hat{B}$  is the magnetic field direction, and  $\theta$  is the shock-field angle, i.e., the angle between the magnetic field direction and the shock normal. The relationship between the particle intensity in the mixed frame and that in the solar wind frame can be written as

$$j_m(\hat{n}) = j'(\hat{n}) + n \frac{U_n \sec \theta v}{c^2} \hat{B} \cdot \hat{n}, \quad (3.7)$$

where  $j_m$  stands for particle intensity in the mixed frame. The cosmic ray intensity in the mixed frame can be written in terms of that in the Earth frame as

$$j_m(\hat{n}) = j_E(\hat{n}) - n\gamma \left( \frac{\vec{V}}{v} \right) \cdot \hat{n} + n \left( \frac{U_n \sec \theta}{c} \right) \left( \frac{v}{c} \right) \hat{B} \cdot \hat{n}, \quad (3.8)$$

where subscripts  $m$  and  $E$  indicate the mixed frame and Earth frame, respectively. Therefore, the anisotropy in the mixed frame can be written in terms of that in the Earth frame as

$$\vec{\xi}_m = \vec{\xi}_E - \frac{n\gamma \vec{V}}{v} + n \left[ \frac{U_n \sec \theta}{c} \right] \left( \frac{v}{c} \right) \hat{B}, \quad (3.9)$$

where  $\vec{\xi}_m$  is the anisotropy vector in the mixed frame, and  $\vec{\xi}_E$  is the anisotropy vector in the Earth frame. For this work, Professor John W. Bieber kindly provided information on GCR data obtained by various neutron monitors in the year 2001. The hourly data include time in units of Day of Year (DOY), GCR intensity ( $j$ ), magnetic fields, anisotropy components ( $\xi_x, \xi_y, \xi_z$ ), and the Kp index. Figure 3.2 displays the GCR intensity versus time. We can clearly identify many Forbush decreases that occurred throughout the year, which was during the period of solar maximum. The spikes shown in Figure 3.2 were explained by Bieber et al. (2004). Solar wind data such as the solar wind velocity are obtained from ACE spacecraft online data [<http://www.srl.caltech.edu/ACE/ASC/level2/index.html>].

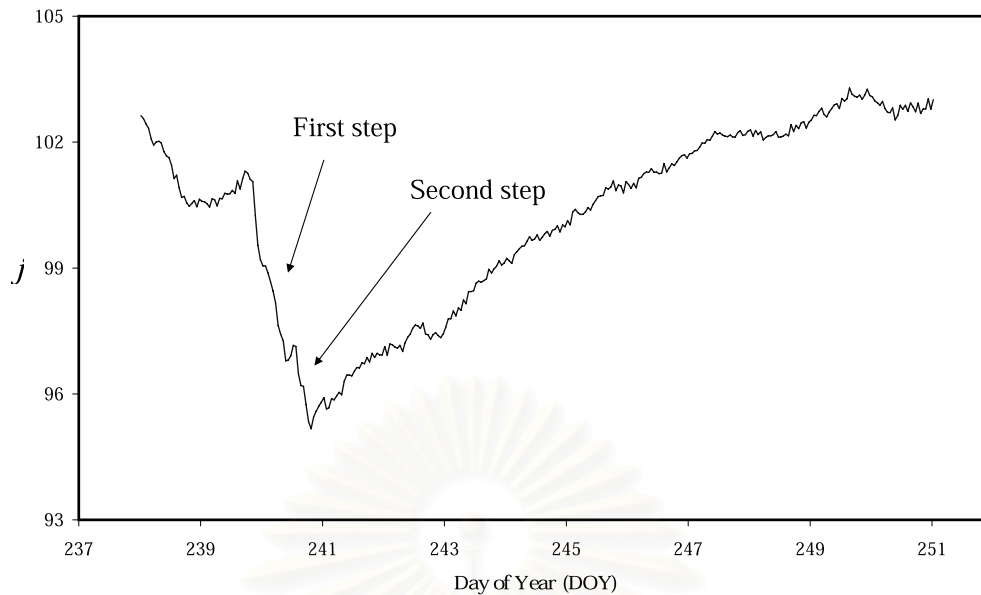


Figure 3.3: GCR intensity ( $j$ ) versus time during DOY 238 to 251 in the year 2001. [Data provided by J. W. Bieber, 2003.]

After the analysis was performed, the results can be summarized as follows:

1) Let us examine Equation 3.8. For the NM data, roughly from DOY 2 to DOY 357 (excluding many days because no solar wind data were available, particularly during the first steps of Forbush decreases), the average Compton-Getting anisotropies in the  $y$ - and  $z$ - directions are -0.001 and -0.005, respectively, and that in the  $x$ -direction (toward the Sun) is -0.403, varying between -0.290 and -0.738.

2) Now we turn to the second term. For a specific event, we chose the first step of the Forbush decrease during DOY 239 to 240 as shown in Figure 3.3. This is the only FD (for year 2001) with available solar wind data. To find the anisotropy in the mixed frame, we found the unit normal vector of the shock shown in Equation 3.10 by assuming magnetic coplanarity, i.e., that the

upstream and downstream magnetic field lines are in a plane [Abraham-Shrauner, 1972; Colburn & Sonett, 1966; Spreiter et al., 1966]:

$$\hat{n} = \frac{\pm(\vec{B}_1 \times \vec{B}_2) \times (\vec{B}_1 - \vec{B}_2)}{|(\vec{B}_1 \times \vec{B}_2) \times (\vec{B}_1 - \vec{B}_2)|}, \quad (3.10)$$

where  $B_1$  and  $B_2$  represent the magnetic field upstream and downstream, respectively (see Figure 3.1). We obtained the shock-field angles of 53.6 degrees upstream and 72.3 degrees downstream. By using the upstream shock-field angles with the measured shock velocity of 300 km/s with respect to the solar wind, the enhanced or depressed NM anisotropy is  $\sim 0.17\%$  along the magnetic field direction. In addition, if the shock-field angle is 76 degrees (i.e., for a quasi-perpendicular shock), the enhancement is about 0.4%.

In conclusion, both terms are of the same order of magnitude. These effects are not completely negligible, but are small compared with typical FD anisotropies of  $\sim 10\text{-}25\%$ .



# Chapter 4

## Loss Cone Precursors and Advance Prediction of Space Weather

### 4.1 Forbush Decrease Precursors and Space Weather Effects

CMEs that have effects on earth could be classified into 3 categories, according to their images in a white-light coronagraph where light from the Sun is blocked by an occulter [Brueckner et al., 1998].

1. A halo event has a more or less symmetrical ring image around the occulter. Halo CMEs expand symmetrically in the plane of the sky. They originate from the center of the Sun within a circle of about 30 degrees.
2. Semi-halo events can be seen as a semi-circle around the occulter extending less than 360 degrees. They propagate non-symmetrically in the plane of

the sky, relative to the occulter.

3. Toroidal CMEs show ejecta simultaneously over the east and the west limb of the Sun, but they are concentrated in the solar equatorial plane. Because of their symmetric appearance over the east and the west limb, one can conclude that they are  $2\pi$  toroids all around the Sun and expand in all directions. Evidently their Earth directed shocks occur in association with erupting filaments.

Shocks and solar energetic particles (SEPs) released from and accelerated at solar active sites can cause variations in Earth's magnetic field and in Earth's atmosphere, such as in the ionosphere. The effects of such variations on human activities are called "space weather effects." Magnetic field variations can cause problems for attitude control of spacecraft and for compass usage. Ionospheric variations include the following: Induction of electrical currents in the Earth that affect power distribution systems, long communication cables, and pipelines; interference with geophysical prospecting; sources for geophysical prospecting; wireless signal reflection, propagation, and attenuation; communication satellite signal interference, scintillation. Problems in the upper atmosphere are low altitude satellite drag and attenuation and scattering of wireless signals.

Solar activity associated with CMEs releases radio waves, known as solar radio bursts, which can cause excess noise in wireless communications systems. Solar radiations released in association with CMEs can affect electronic devices on spacecraft, such as solar cells and other semiconductor devices, including spacecraft charging on surface and interior materials. Solar energetic particles also increase astronaut risks in space and airline passenger risks.

CMEs occur more frequent during times of solar maximum. They are usually difficult to detect by telescopes. Instruments on spacecraft are the only devices to identify CMEs and their shocks. To determine whether or not they are headed toward the Earth, and at approximately what time the impact is expected, a satellite near Earth such as the Advanced Composition Explorer (ACE) acts as a space weather station while in orbit. ACE can provide a one-hour advance warning of any geomagnetic storms that would affect the Earth.

Ground-based observations of cosmic rays by neutron monitors and muon detectors could show precursory anisotropies many hours before the arrival of an interplanetary shock and subsequent FD. This could provide a better way to predict space weather. Precursory anisotropies are interpreted as kinetic effects related to interaction between cosmic rays and the shock [Nagashima et al., 1994; Belov et al., 1995; Morishita et al., 1997; Bieber & Evenson, 1998; Ruffolo et al., 1999]. Precursory decreases are believed to result from a “loss cone” effect, in which a neutron monitor station or muon detector is magnetically connected to the cosmic ray depleted region downstream of the shock. Precursory increases also result from particles reflecting from the approaching shock [Dorman et al., 1995].

Gosling et al. (1990) and Belov et al. (2001) identified 14 major geomagnetic storms observed by a network of neutron monitors with a peak Kp index of 8– or greater. Eleven observed precursors are found out of 14 major storms (79%). Munakata et al. (2000) identified 22 large geomagnetic storms observed by muon detectors. Fifteen observed precursors were found out of 22 events (68%). From these observations, it was found that lead times are 8 hours for muon detectors and 4 hours for neutron monitors. Note that both neutron

monitors and muon detectors measure the intensity of secondary particles produced by the interactions of primary cosmic rays, mostly protons, with atoms in Earth's atmosphere. The typical primary cosmic ray energy producing the secondaries modulated by Forbush decreases is  $\sim 10$  GeV for neutron monitors and  $\sim 30$  GeV for muon detectors.

Figure 4.1 shows a representative power spectrum of interplanetary magnetic turbulence, including typical resonant wave numbers for primary cosmic rays detected by means of atmospheric secondary neutrons ( $n$ ) or muons ( $\mu$ ). Because the typical resonances for neutron monitor and muon detector primaries are in the transition region between energy range and inertial range behavior, the local power-law index varies comparatively rapidly with wave number  $k$ . This power-law index,  $q$ , of the reduced power spectrum as a function of wavenumber is well known to affect the transport of cosmic rays [Jokipii, 1966]. Cosmic rays of  $\sim 30$  GeV, to which a muon detector is sensitive, experience a substantially lower  $q$  value than cosmic rays at  $\sim 10$  GeV, as measured by neutron monitors.

This chapter explains precursors to FDs by performing time-dependent numerical simulations of particle transport near a planar shock using a pitch angle transport equation in a common mathematical framework of Ruffolo (1999). The simulations can indeed explain the lead times for both neutron monitors and muon detectors, and can examine how the shock geometry and spectral index of interplanetary turbulence,  $q$ , affect the angular width of the loss cone precursor and the length scale over which it can be observed.

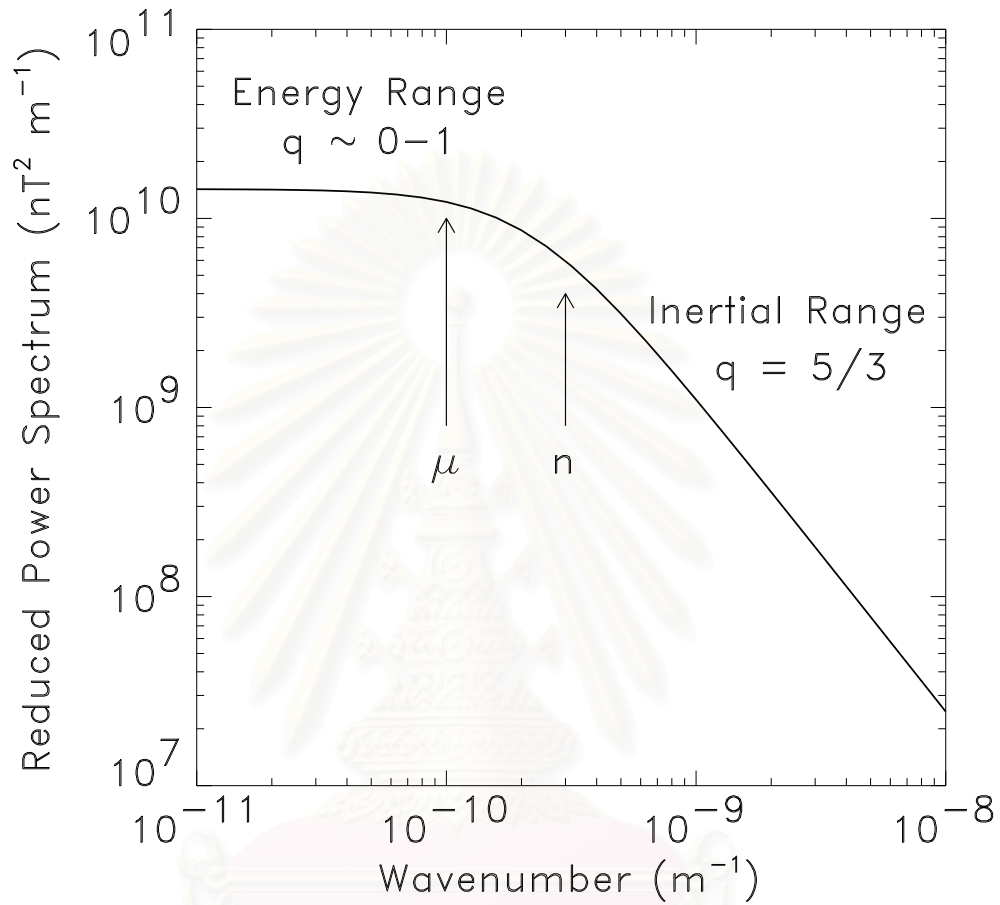


Figure 4.1: Representative power spectrum of interplanetary magnetic turbulence, showing typical resonant wavenumbers for neutron monitor energies (“n”) and for muon detector energies (“μ”). The neutron monitor resonance is almost exactly at the turbulence correlation scale,  $k = \lambda_c^{-1} \approx 3 \times 10^{-10} \text{ m}^{-1}$ . The model spectrum is from equation (13) of Bieber et al. (1994).

## 4.2 Model

### 4.2.1 Transport Equation

The transport equation used in this work is a Fokker-Planck equation of transport that includes the effects of interplanetary scattering and solar wind convection to first order in the solar wind speed [Ruffolo, 1995], incorporating the changes in the pitch angle and momentum as a particle crosses or is reflected by an oblique shock, i.e., a shock oriented at an arbitrary angle with respect to the mean magnetic field.

It turns out that both precursory increases and decreases can be interpreted in terms of a simple model of an oblique, plane-parallel shock with straight magnetic field lines on either side [Ruffolo, 1999]. Consider the de Hoffmann-Teller reference frame in which the shock is stationary, the fluid flow is parallel to the magnetic field, and the electric field is zero [de Hoffmann & Teller, 1950] as shown in Figure 3.1. In this reference frame, the first-order Fermi and shock drift mechanisms are combined into a single mathematical framework. The pitch-angle transport equation of Ruffolo (1995) simplifies to

$$\frac{\partial F}{\partial t} = -\frac{\partial}{\partial z} \left[ \mu v + \left( 1 - \mu^2 \frac{v^2}{c^2} \right) u \right] F + \frac{\partial}{\partial \mu} \left[ \frac{\varphi}{2} \frac{\partial}{\partial \mu} \left( 1 - \mu \frac{uv}{c^2} \right) F \right], \quad (4.1)$$

where  $F(t, z, \mu, p) \equiv d^3N/(dz d\mu dp)$  is the distribution function of particles in a magnetic flux tube,  $t$  is time in the shock (de Hoffmann-Teller) frame,  $z$  is distance from the shock along the magnetic field in the shock frame,  $\mu$  is the cosine of the pitch angle in the local fluid frame (the pitch angle is the angle between the particle velocity and the local magnetic field),  $p$  is the momentum in the local fluid frame,  $v$  is the particle speed in the local fluid frame,  $u = u_n \sec \theta_{Bn}$  is the fluid speed along the field relative to the shock,  $u_n$  is the fluid speed normal



to the shock,  $\theta_{Bn}$  is the angle between the magnetic field and the shock normal, and  $\varphi(\mu)$  is the pitch angle scattering coefficient. A similar transport equation was employed to study ultrarelativistic particle acceleration [Kirk & Schneider, 1987] and to examine the effect of the form of  $\varphi(\mu)$  [Kirk, 1988]. In the present work, the sign conventions for  $z$  and  $\mu$  are as follows:  $z$  increases toward the upstream direction,  $z > 0$  for locations upstream of the shock (outward from the Sun, in the case of a Forbush decrease), and  $z < 0$  for locations downstream of the shock. Similarly,  $\mu > 0$  for motion in the upstream direction in the fluid frame. For consistency with the above we have  $u < 0$ , i.e., fluid flow from upstream to downstream in the shock frame.

We use the following form of the pitch angle scattering coefficient [Jokipii, 1971]:

$$\varphi(\mu) = A|\mu|^{q-1}(1 - \mu^2), \quad (4.2)$$

where the parameter  $A$  can be related to  $\lambda$ , the parallel mean free path for interplanetary scattering, by the well-known expression:

$$\frac{v}{A} = \frac{(2 - q)(4 - q)}{3}\lambda, \quad (4.3)$$

and  $q$  characterizes the steepness of a presumed power spectrum of interplanetary magnetic turbulence varying with wavenumber  $k$  as  $|k|^{-q}$ . In equation (4.2), any value of  $q < 1$  leads to enhanced pitch angle diffusion at  $\mu = 0$  (a pitch angle of  $90^\circ$ ), and a flatter pitch angle distribution near  $\mu = 0$ , whereas  $q > 1$  leads to less pitch angle diffusion and a steeper gradient of the pitch angle distribution near  $\mu = 0$ . Since the observed power spectrum is typically similar to that shown in Figure 4.1, with an effective spectral index  $q$  that varies with wavenumber and hence with particle energy, we perform simulations of cosmic ray pitch angle transport near a shock for various values of  $q$ .



## 4.2.2 Numerical Simulations

We model upstream precursors of Forbush decreases by solving equation 4.1 for the time-dependent distribution of Galactic cosmic rays near an oblique, interplanetary shock. Physically, we consider that Forbush decreases downstream of a shock result because the fresh downstream plasma emitted along with a CME has a relatively low density of Galactic cosmic rays, and their flow into this downstream plasma is inhibited by particle reflection at the shock. (Our particle orbit simulations show that even for a magnetic compression ratio as low as 1.5, a majority of energetic particles coming from upstream are reflected.) Therefore, we assume that the particle distribution function is initially constant with a constant inflow upstream, and initially constant at half that density downstream.

We performed time-dependent simulations of Galactic cosmic rays with varying magnetic field-shock angle and  $q$ , considering protons with a momentum of  $p = 25 \text{ GeV } c^{-1}$ , a value intermediate between typical energies of particles detected by neutron monitors and muon detectors. For highly relativistic particles (such as cosmic rays measured by either neutron monitors or muon detectors), the exact value of  $p$  has little effect on the simulation results. The separable solutions depend on  $u/v$ , which in this case is nearly constant at  $\approx u/c$ , and shock encounters result in a fractional momentum increase that is independent of  $p$ . The grid spacings in the simulations were  $\Delta\mu = 2/45$  and  $\Delta z/\lambda = 0.05$ , with  $v\Delta t/\Delta z = 0.4\lambda$ . (Recall that  $z$  refers to the distance from the shock along the magnetic field, and  $\lambda$  is the parallel mean free path.) Outer boundaries were placed at  $\pm 8\lambda$  from the shock. A spectral index of 2.7 was assumed; the simulation results were found to be insensitive to this value. We allowed the simulations to evolve for a constant simulation time chosen to yield a typical

peak-to-minimum anisotropy of a few percent in the near upstream region, in accord with observations (e.g., Nagashima et al., 1992). Results presented below are based upon the simulated spatial and pitch angle distribution of cosmic rays at this instant of time. There was very little difference in the results when comparing simulations evolved to a constant peak-to-minimum anisotropy.

At this stage we do not expect to accurately model the Forbush decrease itself, downstream of the shock, since we do not yet take into account the evolution of the shock as it moves outward, the presence of CME ejecta, etc. Nevertheless, we consider this a plausible model of the upstream precursors, because the distribution function upstream is mainly affected by a deficit of particles in the fresh plasma downstream, and not as much by the detailed conditions there.

The numerical methods are based on those of Ruffolo (1999) and Nutaro et al.(2001). One significant modification is that while Ruffolo (1999) assumed that pitch angle changes at an oblique shock conserve the adiabatic invariant,  $p_{\perp}^2/(2meB) \propto (1 - \mu^2)/B$  (the magnetic moment), we now consider particle orbits as they cross the shock, using a transfer matrix to assign the distribution function to the appropriate  $\mu$  and  $z$  cells after the shock encounter. In principle, the treatment of particle orbits should be more accurate than the assumption of conservation of the adiabatic invariant. In any case, we have found that results of the present work are essentially the same for both numerical treatments, for a variety of shock-field angles.

Note that following Ng & Wong (1979), Equation 4.1 is expressed in terms of  $F$ , the distribution function of particles in a magnetic flux tube. We present results in terms of the particle intensity  $j$ , where the two quantities are related by  $F = 2\pi A j$ , and  $A(z)$ , the area of the flux tube, is inversely proportional to

the magnetic field strength  $B$ . [The intensity  $j$  is in turn related to the phase space density  $f$  by  $j = p^2 f$ .] We normalize the results so that  $j$  averaged over  $\mu$  is unity at the far downstream boundary.

### 4.3 Results

The numerical simulations yield the particle intensity  $j$  as a function of  $\mu$ , the pitch angle cosine in the local fluid frame, and  $z$ , the distance from the shock along the magnetic field in units of the mean free path,  $\lambda$ . Figure 4.2 shows sample distributions for  $\tan \theta_{Bn} = 4$ , i.e.,  $\theta_{Bn} = 76^\circ$  (recall that  $\theta_{Bn}$  is the angle between upstream magnetic field lines and the shock normal). The upper panel is for  $q = 0.5$  and the lower panel is for  $q = 1.0$ , close to the values appropriate for muon detectors and neutron monitors, respectively. The contours represent levels of equal particle intensity. For  $\mu > 0$ , particles are moving in the upstream direction (away from the Sun), and for  $\mu < 0$  particles are moving downstream (toward the Sun).

In both panels, we see significant changes in the pitch angle distribution near the shock (at  $z = 0$ ). While particles moving with  $\mu \approx -1$  flow from the upstream to the downstream side of the shock, particles with slightly higher  $\mu$  are reflected, causing the increase in intensity for  $\mu$  slightly greater than zero. Effectively, the shock is a barrier to the particle propagation, damming the flow from upstream to downstream and causing the Forbush decrease downstream. The key difference between the results for  $q = 0.5$  and  $q = 1$  is the shape of the pitch angle distribution,  $j$  vs.  $\mu$ , which is flattened near  $\mu = 0$  in the former case due to enhanced scattering at a pitch angle of  $90^\circ$  (see Section 4.1). At higher  $\mu$  values, close to  $\mu = 1$ , we are seeing particles that flow from downstream of the

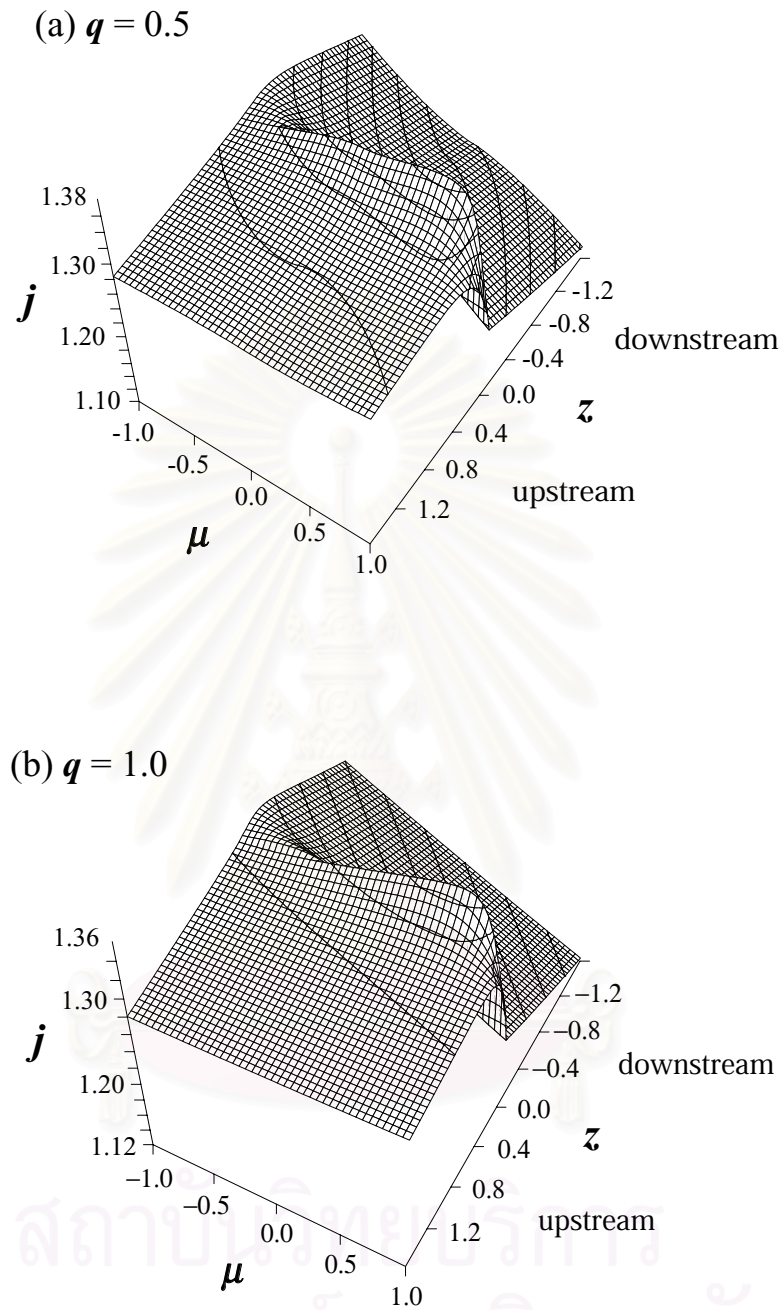


Figure 4.2: Intensity distribution,  $j$ , of Galactic cosmic rays as a function of  $\mu$  and  $z$  (in units of  $\lambda$ ) near an oblique shock with  $\theta_{Bn} = 76^\circ$  for (a)  $q = 0.5$  and (b)  $q = 1.0$ .

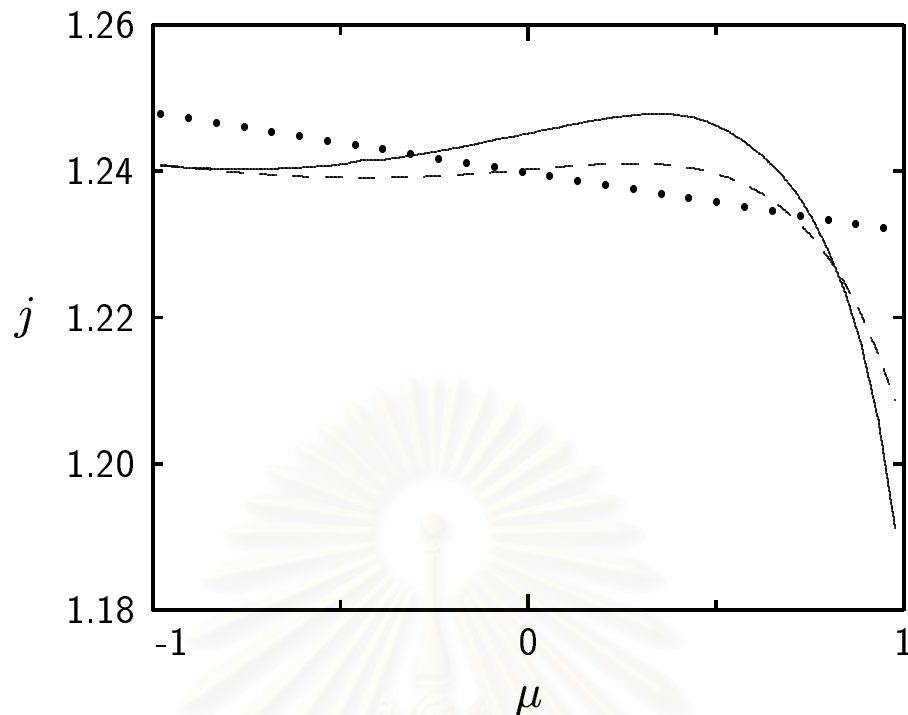


Figure 4.3: Simulated Galactic cosmic ray intensity as a function of  $\mu$  near an oblique interplanetary shock at  $z = 0.025\lambda$  (solid line),  $z = 0.125\lambda$  (dashed line), and  $z = 1.575\lambda$  (dotted line) for  $\theta_{Bn} = 76^\circ$  and  $q = 1$ .

shock to the upstream side. Because of the deficit of particles downstream, there is a corresponding precursory decrease on the upstream side, for a narrow cone of directions around the magnetic field line, comprising the “loss cone.” This is a distinctive anisotropy feature that is readily observable by ground-based neutron monitors and muon detectors. At a given time, networks of detectors on the Earth measure the directional distribution of the Galactic cosmic rays, i.e.,  $j$  as a function of  $\mu$  at fixed  $z$ , corresponding to a slice through Figure 4.3. Such pitch angle distributions are shown in Figure 3 for various distances from the shock, at  $\tan \theta_{Bn} = 4$  and  $q = 1$ . At the earliest time, when the shock is greater than a mean free path away, an observer sees at most a diffusive anisotropy (dotted line in Figure 4.3). As the shock moves closer to an intermediate distance (dashed line) or

small distance (solid line), we see the solution with increasing strength, exhibiting both the loss cone decrease near  $\mu = 1$  and the shock reflection increase just above  $\mu = 0$ . Thus these precursors signal the imminent arrival of an interplanetary shock.

To be more precise, Leerunnavarat et al. (2003) pointed out that the solution decays exponentially with increasing distance from the shock. Indeed, the steady-state distribution function is a superposition of separable solutions, each with a different decay length. Like Ruffolo (1999), we have found that the same separable solutions are recognizable in the results of time-dependent simulations, but with decay lengths that are somewhat different. Therefore, we have fit our simulation results to determine these decay lengths numerically to be used as an indicator of the lead time for advance warning of the arrival of an interplanetary shock.

Ruffolo (1999) and Leerunnavarat et al. (2003) examined separable solutions of Equation 4.1 for a steady state. Each separable solution has a non-zero contribution to the omnidirectional density of cosmic rays,  $\langle j \rangle_\mu$ , as a function of  $z$  upstream of the shock. We can fit this to the sequence

$$\langle j \rangle_\mu = a_0 + a_1 e^{-z/\ell_1} + a_2 e^{-z/\ell_2} + \dots, \quad (4.4)$$

where  $a_i$  is the coefficient of each separable solution and  $\ell_i$  is the corresponding decay length. The first term in Equation (4.4) corresponds to the solution far upstream, i.e., the quiet-time density of Galactic cosmic rays, the second term is a diffusive solution that decays over  $\ell_1 = D/u$  from the shock, and the higher order terms appear closer and closer to the shock. Here we fitted our simulation results up the second term, which is sufficient for extracting  $\ell_2$ ,



the decay length of the loss cone feature. Indeed, our simulations had insufficient spatial resolution to resolve higher-order features.

Table 4.1 summarizes the decay length of loss cone features as derived from our simulations for varying  $q$  and  $\theta_{Bn}$ , including both quasi-parallel and quasi-perpendicular shock configurations. Note that we do not expect the decay length from our time-dependent simulations to exactly correspond to the steady-state result. In a steady state,  $\ell/\lambda$  depends only on  $q$  and rather weakly on  $|u_n| \sec \theta_{Bn}/v$ . On the other hand, in more realistic time-dependent simulations it has a substantial variation with both  $q$  and  $\theta_{Bn}$ . As shown in Figure 4.4a, the decay length (and hence the lead time in space weather forecasting) decreases substantially with increasing  $q$ , in qualitative agreement with the steady-state theory.

We also see that the decay length is much longer for quasi-perpendicular shocks than for quasi-parallel shocks. This circumstance is rather fortunate, because loss cones from quasi-perpendicular shocks will generally provide less advance warning of shock arrival by virtue of the geometric relation  $\Delta r = \Delta z \cos \theta_{Bn}$  (assuming radial shock propagation). The increase of  $\ell/\lambda$  with  $\theta_{Bn}$  partially counteracts this. Figure 4.4b plots as a function of  $q$  the ratio  $\ell \cos \theta_{Bn}/\lambda$ , which determines the lead time of a loss cone precursor in the case of radial propagation (cf. eq. [4.5]). There is less overall spread in this quantity than in  $\ell/\lambda$  (Figure 4.4a), and the shape of these curves evolves more smoothly with  $\theta_{Bn}$ . (Note also that we estimate an uncertainty in the  $\ell$  values on the order of 10%, and not less than  $0.01\lambda$ .) We see that the intermediate shock-field angles provide the longest lead time for space weather forecasting.

Finally, our simulations can also address the angular width of the loss



Table 1: Angular Width and Decay Length of Loss Cone Features. [<sup>a</sup> denotes the decay length of the loss cone feature, in units of  $\lambda$ , <sup>b</sup> taken from Leerunnavarat et al., 2003.]

$q$	$\tan \theta_{Bn}$	$\theta_{Bn}$ (degrees)	$\theta_{HW}$ (degrees)	$\ell/\lambda^a$ (simulation)	$\ell/\lambda^a$ (steady state) <sup>b</sup>
0.1	0.10	5.71	45.1	0.11	0.239
0.1	0.25	14.04	42.5	0.14	0.239
0.1	0.50	26.56	32.8	0.19	0.239
0.1	1.00	45.00	25.4	0.24	0.239
0.1	4.00	75.96	24.8	0.25	0.238
0.5	0.10	5.71	49.3	0.08	0.195
0.5	0.25	14.04	44.3	0.13	0.195
0.5	0.50	26.56	33.4	0.17	0.195
0.5	1.00	45.00	25.9	0.21	0.195
0.5	4.00	75.96	24.8	0.23	0.194
1.0	0.10	5.71	57.2	0.05	0.137
1.0	0.25	14.04	46.8	0.11	0.137
1.0	0.50	26.56	34.7	0.14	0.137
1.0	1.00	45.00	26.9	0.17	0.137
1.0	4.00	75.96	24.8	0.21	0.137
1.5	0.10	5.71	68.3	0.03	0.073
1.5	0.25	14.04	50.3	0.07	0.073
1.5	0.50	26.56	37.1	0.09	0.073
1.5	1.00	45.00	29.6	0.11	0.073
1.5	4.00	75.96	25.0	0.17	0.073

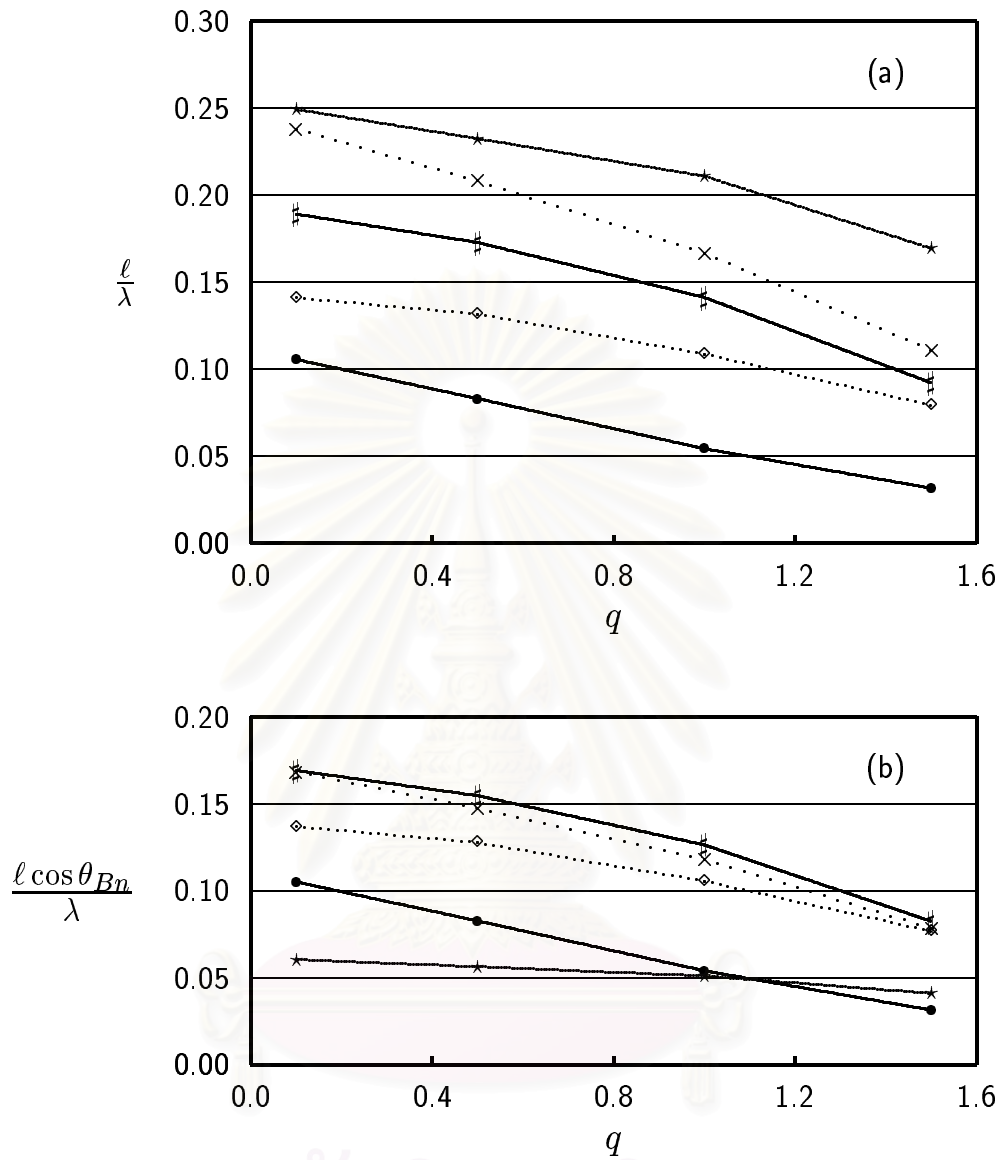


Figure 4.4: (a) Loss cone decay length,  $\ell$  (in units of  $\lambda$ ), as a function of  $q$  for shock-field angles  $\theta_{Bn} = 5.7^\circ$  ( $\bullet\text{---}\bullet$ ),  $14.0^\circ$  ( $\diamond\cdots\diamond$ ),  $26.6^\circ$  ( $\#\text{---}\#$ ),  $45.0^\circ$  ( $\times\cdots\times$ ), and  $76.0^\circ$  ( $\star\text{---}\star$ ). (b) The quantity  $\ell \cos \theta_{Bn} / \lambda$ , which determines precursor lead time in the case of radial shock propagation, as a function of  $q$  for the same shock-field angles.

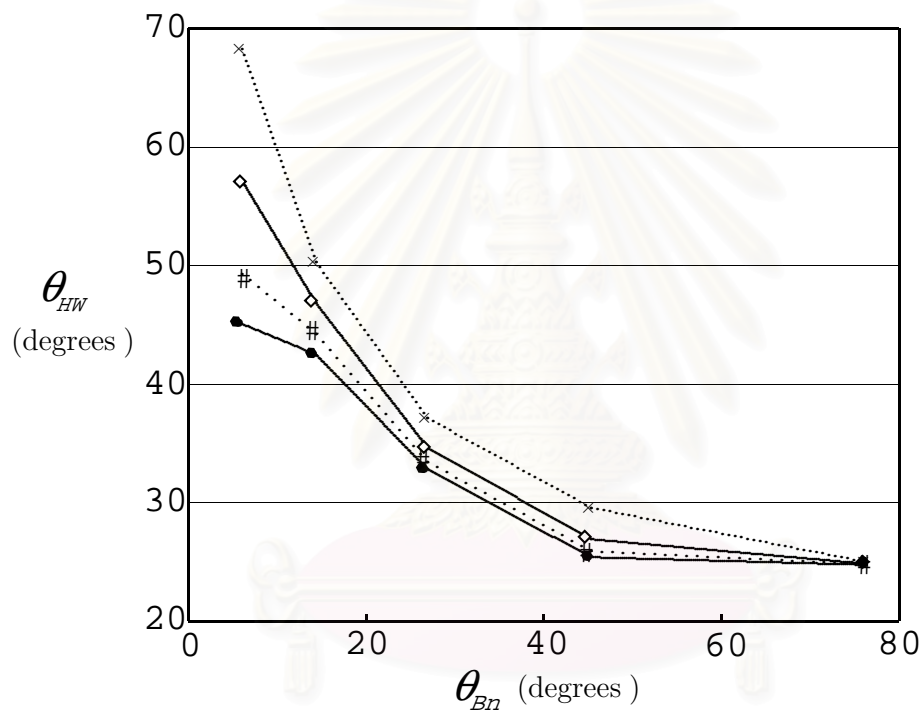


Figure 4.5: Loss cone opening angle,  $\theta_{HW}$ , as a function of the shock-field angle  $\theta_{Bn}$  for  $q = 0.1$  ( $\bullet\text{---}\bullet$ ),  $0.5$  ( $\#\cdots\#$ ),  $1.0$  ( $\diamond\text{---}\diamond$ ), and  $1.5$  ( $\times\cdots\times$ ).

cone, which in principle can be observed by ground-based cosmic ray detectors. Here the loss cone width is defined by the point at which the intensity decrease (relative to the omnidirectional intensity  $\langle j \rangle_\mu$ ) has reached half its maximum value. In three dimensions, this indicates the half-width opening angle of the loss cone, and we denote it as  $\theta_{HW}$ . The determination of loss cone width is made in the near upstream region, specifically  $z = \lambda/40$ . This quantity is also given in Table 4.1 for various  $q$  and  $\theta_{Bn}$ . As shown in Figure 4.5, the loss cone opening angle tends to decrease with the shock-field angle. For a low shock-field angle (quasi-parallel shock), the width increases with increasing  $q$ , but the width tends to be independent of  $q$  for a high shock-field angle (quasi-perpendicular shock).

## 4.4 Discussion

In this section, we use our results to estimate the expected lead time for loss cones observed by muon detectors and neutron monitors, i.e., the time of advance warning before the arrival of an interplanetary shock. Both detector types respond to a broad range of energies, with the median energy of response being  $\sim 60$  GeV for a muon detector and  $\sim 17$  GeV for a high-latitude neutron monitor. Shock interactions with ambient cosmic rays, however, disproportionately affect the particles of lower energy. The depth of a Forbush decrease, for instance, varies inversely with energy for the energies under consideration here [Morishita et al., 1990]. From these considerations, we adopt 30 GeV and 10 GeV, respectively, for the effective energies of cosmic rays measured by a muon detector and neutron monitor when observing a loss cone.

Two important factors differentiate muon detectors and neutron monitors for purposes of estimating the expected loss cone decay length. First, the

particles they detect have different scattering mean free paths. Second, and less obvious, the particles are resonant with different ranges of the turbulence spectrum corresponding to different spectral indices  $q$ , where  $q$  is the exponent of a presumed power law spectrum varying with wavenumber  $k$  as  $|k|^{-q}$ .

From an analysis of the detailed shape of the cosmic ray pitch angle distribution measured by neutron monitors, Bieber & Pomerantz (1983) determined that a spectral index  $q = 1.1$  and a mean free path  $\lambda_{\parallel} = 0.5$  AU describe the data well, for an effective cosmic ray energy of 10 GeV. The mean free path is consistent with the value  $\sim 1$  AU at the slightly higher energy (17 GeV) obtained by analysis of cosmic ray streaming and gradients [Chen & Bieber, 1993].

The value  $q = 1.1$  is reasonably consistent with the typical value  $q \sim 1.2$  derived from direct measurement of the IMF power spectrum in the low-frequency regime of relevance to neutron monitor energies [Bieber et al., 1993]. Further, it is consistent with current understanding of the turbulence power spectrum. Ten GeV cosmic rays are resonant with fluctuation scales near the turbulence correlation length, as illustrated in Figure 4.1. To compute a representative resonant wavenumber, we use  $k_{res} = (R_L \cos \theta)^{-1}$ , with pitch angle  $\theta = 45^\circ$  and with the Larmor radius  $R_L$  computed for a 5 nT magnetic field. For the effective cosmic ray energy measured by neutron monitors (indicated by  $n$  in Figure 4.1), the resonant wavenumber almost exactly equals the inverse of the turbulence correlation length,  $\lambda_c^{-1} \approx 3 \times 10^{-10} \text{ m}^{-1}$ . At this length scale, the power spectrum is steepening from the comparatively shallow slope ( $q \sim 0 - 1$ ) of the turbulence energy-containing range to the Kolmogoroff slope ( $q = 5/3$ ) of the inertial range. Although the spectrum shown in the figure has a continually changing slope near the correlation scale, a value  $q = 1.1$  is reasonable for comparison with our

Table 2: Estimated Loss Cone Lead Times

Detector	Representative	$q$	$\lambda$	$\ell/\lambda$	$\ell$	$T$
Type	Energy		(AU)		(AU)	(hr)
Neutron Monitor	10 GeV	1.1	0.5	0.16	0.08	4
Muon Detector	30 GeV	0.5	1.5	0.21	0.31	15

simulations, which assume a constant slope.

The appropriate mean free path at cosmic ray energies appropriate for muon detectors is reported to be higher than for neutron monitors [Hall et al., 1997]. This is in accord with theoretical expectation that the mean free path  $\lambda$  should depend upon particle rigidity  $P$  as  $\lambda \propto P^{2-q}$ . With  $q = 1.1$ , this implies a nearly linear relationship. Accordingly, we adopt a value  $\lambda = 1.5$  AU for muon detector measurements, which is simply 3 times the neutron monitor value.

Direct evidence for the value of  $q$  appropriate to muon detectors is lacking. However, based on the general characteristics of turbulence spectra discussed above and illustrated in Figure 4.1, we expect a smaller value of  $q$  than for neutron monitors. Estimates based upon simple model spectra (e.g., Bieber et al. (1994)) lead us to adopt  $q = 0.5$  for muon detector energies.

The representative parameters for the two detector types are listed in Table 4.2. With  $q$  and  $\lambda_{\parallel}$  known, we are now in a position to estimate the ratio  $\ell/\lambda_{\parallel}$  from Figure 4.4. We use the curve for  $\tan(\theta_{Bn}) = 1$ , i.e., a shock normal angle of  $45^\circ$ . These ratios along with the implied value of the decay length  $\ell$  itself are shown in the table. Finally, to convert the decay length to a lead time  $T$  that might be applicable to space weather forecasting, we assume a radially propagating shock, in which case  $T$  is given by

$$T = \frac{\ell \cos \theta_{Bn}}{V_s}, \quad (4.5)$$

where  $V_s$  is the shock speed in Earth's rest frame. For purposes of illustration, we take  $V_s = 600$  km/s and (as previously stated)  $\theta_{Bn} = 45^\circ$ . Equation (4.5) presumes that the loss cone will first be detectable exactly one decay length upstream, though in fact the exact distance will depend upon other factors such as the width and depth of the loss cone, as well as how complete the observing network's directional coverage is.

As shown in the last column of Table 4.2, our estimated lead time is 15 hours for muon detectors and 4 hours for neutron monitors. This is in good agreement with the observational results discussed at the beginning of this chapter. Typical lead times actually observed by muon detectors are indeed somewhat less than our estimate. However, the existing muon detector network has coverage only in the eastern hemisphere (Japan, Australia, and Antarctica). As noted by Munakata et al. (2000), the first detection of a loss cone by muon detectors often occurs when the detector network rotates into the sunward viewing direction. The loss cone may have been present prior to this, but was unobserved owing to gaps in the muon detector network. (Fortunately, sky coverage by the muon detector network is improving thanks to the installation and planned expansion of a muon detector in São Martinho, Brazil. See Munakata et al., 2001.)

Next, let us consider how observations of individual loss cone precursors can in principle indicate the shock arrival time on a case-by-case basis. In Figure 4.3, we see that for large field-shock normal angles,  $\theta_{Bn}$ , i.e., for quasi-perpendicular shocks, the loss cone opening angle  $\theta_{HW}$  is nearly independent of  $q$ . This is even approximately true for  $\theta_{Bn}$  as low as  $\approx 15^\circ$ . Therefore, an observational measurement of  $\theta_{HW}$  gives a fairly good determination of  $\theta_{Bn}$ . (Note, however, that for a parallel shock there should not be a loss cone precursor, as



there is no shock reflection or change in pitch angle as particles cross the shock. For nearly parallel shocks the loss cone is not very deep and may be difficult to observe.) At the very least, there is a robust indication that for a wide loss cone opening angle ( $\gtrsim 45^\circ$ ) the shock is quasi-parallel and that for a narrow loss cone opening angle ( $\lesssim 30^\circ$ ) the shock is quasi-perpendicular.

Observational indications of shock-field angles are of interest in and of themselves; furthermore, they provide a means to estimate the lead time before the shock arrival. If we can estimate the shock-field angle and  $q$ , then we can obtain  $\ell/\lambda$  from Figure 4.4. Assuming for simplicity that the shock normal is in the radial direction, we can estimate the lead time from Equation 4.5. Taking measurement uncertainties into account, this technique can at least give a qualitative indication of whether the shock arrival should be imminent or delayed. With further observations, or testing on historical data, this indication could be calibrated to give quantitative forecasts of the shock arrival time.

## 4.5 Conclusions

To conclude this chapter, we summarize that observed precursors to Forbush decreases can be explained in a mathematical framework of cosmic ray pitch angle transport near an oblique, plane-parallel shock. The loss cone decreases and shock reflection increases should occur in tandem, corresponding to the same separable solution of the transport equation. Numerical simulations of cosmic ray interactions with a CME shock have been performed for various shock-field angles and various values of  $q$ , the power-law index of magnetic turbulence. We point out that different values of  $q$  are appropriate for cosmic rays of different energy ranges, and show that the loss cone precursors to Forbush decreases should

typically be detectable by neutron monitors about 4 hours prior to shock arrival, and by muon detectors about 15 hours prior to shock arrival. The results are consistent with observational surveys and suggest that ground-based cosmic ray detectors can play a useful role in space weather forecasting.

In addition, our work has shown that the width of a precursor loss cone provides a prediction of whether the approaching shock is quasi-parallel or quasi-perpendicular. The quasi-perpendicular shocks produce loss cones with opening angles  $\sim 25^\circ$ , whereas the quasi-parallel shocks have loss cones with opening angles  $\sim 50^\circ$ . This removes another unknown in the estimation of the lead time, and implies that loss cone measurements can in principle provide a quantitative indication of the time when an interplanetary shock will arrive at Earth.



สถาบันวิทยบริการ  
จุฬาลงกรณ์มหาวิทยาลัย

# Chapter 5

## Simulation of Forbush Decreases

This work is the first attempt to model the first step of Forbush decreases without simplified assumptions of analytic formulas for the solar wind and magnetic field by using data from a simulation of CME propagation. The ultimate goal is to be able to obtain a sudden qualitative decrease of GCR density behind the shock (see Figure 2.12). Therefore, the expected results would not give as much detail as those of precursors to Forbush decreases in Chapter 4.

There are two sets of programs for the simulations, i.e., Model I and Model II. Model I requires many new or modified subroutines to derive relevant quantities from inputs resulting from a simulation of a CME. (We received the inputs from Dr. David Lario, Applied Physics Laboratory, Johns Hopkins University, USA. He was using a program developed by M. Vandas from the Astronomical Institute, Academy of Science, Prague, Czech Republic.) In contrast, theoretical analytic formulas are also used in some functions in Model II for comparison. Speculatively, Model I should give more realistic results than those of Model II. Unfortunately, there is a problem with the input files (see Section 5.4), so Model II is hence a better candidate for reaching the goal.

This chapter will summarize the models, both programs and results from Model II.

## 5.1 Transport Equation

The GCR transport equation in this work is also described by a Fokker-Planck equation. Ruffolo & Chuychai (1999) had worked out a general form of the equation of Skilling (1975) with one spatial coordinate. This equation describes the time evolution of a particle distribution function,  $F$ , along a magnetic field line on either side of a plane shock, considering streaming, convection, adiabatic deceleration, scattering and focusing (Equation 5.1).

$$\begin{aligned}
\frac{\partial F(t, z, \mu, p)}{\partial t} = & -\frac{\partial}{\partial z} \left[ U_z + \mu v l_z - \frac{\mu^2 v^2 \vec{U} \cdot \hat{l}}{c^2} l_z \right] F \\
& -\frac{\partial}{\partial p} p \left[ \frac{1 - 3\mu^2}{2} l_i l_j \frac{\partial U_j}{\partial x_i} - \frac{1 - \mu^2}{2} \vec{\nabla} \cdot \vec{U} - \frac{\mu}{v} \hat{l} \cdot \frac{\partial \vec{U}}{\partial t} \right] F \\
& -\frac{\partial}{\partial \mu} \frac{1 - \mu^2}{2} \left[ v \vec{\nabla} \cdot \hat{l} + \mu \vec{\nabla} \cdot \vec{U} - 3\mu l_i l_j \frac{\partial U_j}{\partial x_i} - \frac{v \vec{U}}{c^2} \cdot \frac{\partial \hat{l}}{\partial t} \right. \\
& \quad \left. - \frac{2}{v} \hat{l} \cdot \frac{\partial \vec{U}}{\partial t} - \frac{\mu v^2 \vec{U} \cdot \hat{l}}{c^2} \vec{\nabla} \cdot \hat{l} \right] F \\
& + \frac{\partial}{\partial \mu} \left[ \frac{\varphi(\mu)}{2} \frac{\partial}{\partial \mu} \left( 1 - \frac{\mu v \vec{U} \cdot \hat{l}}{c^2} \right) F \right], \tag{5.1}
\end{aligned}$$

where  $F(t, \mu, z, p) \equiv d^3 N / (d\mu dr dp)$  is the particle distribution function, related to the phase space density,  $f(t, \vec{x}, \vec{p})$ , by  $F = 2\pi r^2 p^2 f$ , and the phase space density is related to the particle density,  $j$ , by  $j = p^2 f$  (see Appendix A). Also,  $\mu$  is the cosine of the pitch angle of particles moving along the magnetic field line,  $v$  is the particle speed,  $\vec{U}$  is the solar wind velocity,  $c$  is the speed of light,  $t$  is time,  $\hat{l}$  is a

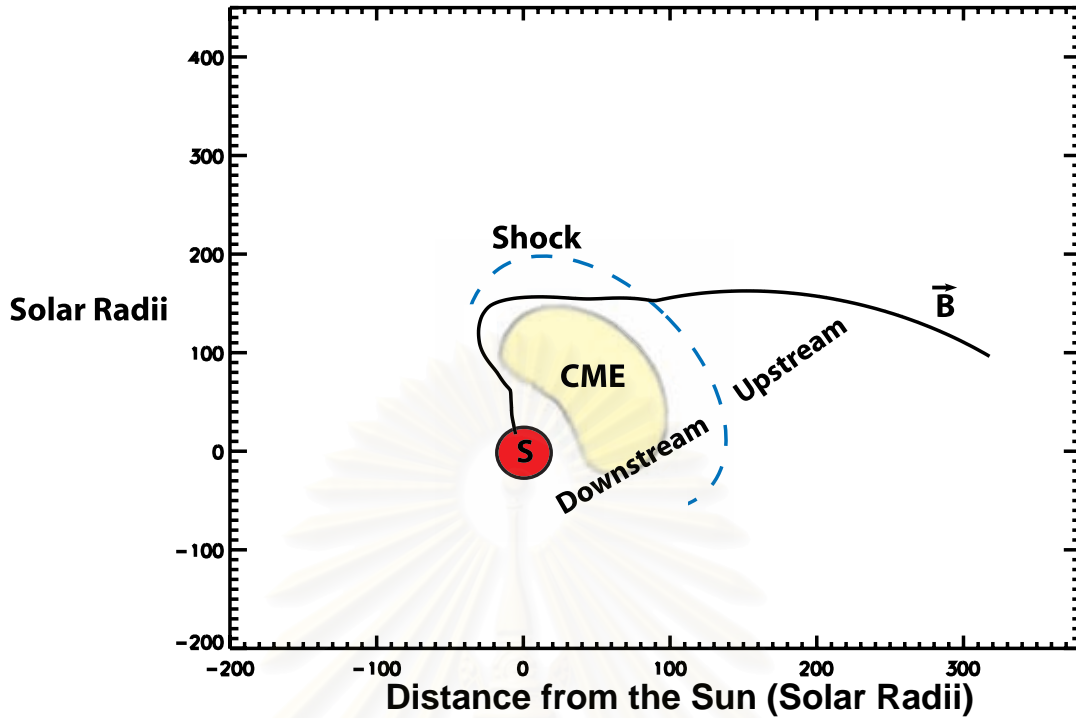


Figure 5.1: The configuration for our Forbush decrease simulation

unit vector along the mean magnetic field line,  $p$  is the magnitude of the particle momentum,  $z$  is a spatial coordinate which this work uses as the radial distance from the Sun, and  $\varphi(\mu)$  is the pitch angle scattering coefficient. The variables  $p$ ,  $\mu$  and  $v$  are defined in the local solar wind frame and others are defined in the solar fixed frame, while the transport of particles across the shock front is done in the de Hoffman-Teller frame in which the electric field is absent [de Hoffman & Teller, 1950]. The quantity  $F$  allows us to use the numerical method of finite differencing to guarantee, in a straightforward manner, the conservation of particle number. The phase space density,  $f$ , is conserved when using the Lorentz Transformation between the frames of reference and  $j$  is the particle density used in reports of real observations.

## 5.2 Numerical Methods

In this work, we solved Equation 5.1 by a finite difference method, specifically, using the *operator splitting technique* which is also called *time splitting* or *the method of fractional steps* [Yanenko, 1971; Press et al., 1988]. This is a powerful technique to handle a complex multi-dimensional linear partial differential equation. A simple explanation of this method is that we solve one term in the equation at a time for a small timestep and a small spatial distance step and repeating the procedure for the whole spatial domain and time domain (see Appendix B). Equation 5.1 could be separated into 3 parts according to derivatives with respect to  $z$ ,  $\mu$  and  $p$ , i.e.,

$$\begin{aligned} \frac{\partial F}{\partial t} = & -\frac{\partial}{\partial \mu} \frac{1-\mu^2}{2} \left[ v \vec{\nabla} \cdot \hat{l} + \mu \vec{\nabla} \cdot \vec{U} - 3\mu l_i l_j \frac{\partial U_j}{\partial x_i} - \frac{v \vec{U}}{c^2} \cdot \frac{\partial \hat{l}}{\partial t} \right. \\ & \left. + \frac{\partial}{\partial \mu} \left[ \frac{\varphi(\mu)}{2} \frac{\partial}{\partial \mu} \left( 1 - \frac{\mu v \vec{U} \cdot \hat{l}}{c^2} \right) F \right] \right] \end{aligned} \quad (5.2)$$

$$\frac{\partial F}{\partial t} = -\frac{\partial}{\partial p} p \left[ \frac{1-3\mu^2}{2} l_i l_j \frac{\partial U_j}{\partial x_i} - \frac{1-\mu^2}{2} \vec{\nabla} \cdot \vec{U} - \frac{\mu}{v} \hat{l} \cdot \frac{\partial \vec{U}}{\partial t} \right] F \quad (5.3)$$

$$\frac{\partial F}{\partial t} = -\frac{\partial}{\partial z} \left[ U_z + \mu v l_z - \frac{\mu^2 v^2 \vec{U} \cdot \hat{l}}{c^2} l_z \right] F. \quad (5.4)$$

Then, we update  $F$  in sequential steps as:

1. Update  $F$  for  $\mu$ -changing processes over a time  $\Delta t/2$ .
2. Update  $F$  for  $p$ -changing processes over a time  $\Delta t$ .
3. Update  $F$  for  $z$ -changing processes over a time  $\Delta t$ .
4. Update  $F$  for  $\mu$ -changing processes over a time  $\Delta t/2$ .

Note that  $\mu$ -changing processes were treated twice at the beginning and at the end because their symmetric treatment helps in improving the method to second order convergence in  $\Delta t$ .

The transport equation was solved on either side of the shock, i.e., the upstream region where the shock has not arrived and the downstream region where the shock has passed already (see Figure 5.1). At the shock, we used particle orbit calculations about the guiding center to find whether the particles of some certain pitch angles and gyrophases are able to cross the shock. Originally, the orbit calculation program, also called the orbit code, needed to be run separately from the main program because it was written in Fortran by Dr. Nuanwan Sanguansak [Sanguansak & Ruffolo, 1999; Leerungnavarat et al., 2000]. This work has been able to incorporate the Fortran orbit codes with the main program in the C language (see Appendix C).

## 5.3 Numerical Simulations

### 5.3.1 Model I

In Model I, we apply the transport equation to our situation where the magnetic field line is curved around a CME and is kinked at the shock as shown in Figure 5.1. The magnetic field line seen in the Figure was generated by a simulation of CME propagation in the inner heliosphere in two dimensions by Dr. David Lario at the Applied Physics Laboratory, Johns Hopkins University, using a program provided by M. Vandas. The CME simulation was done in spherical coordinates, providing information about the magnetic field and solar wind, i.e., with radial and azimuthal components of both the magnetic field and solar wind denoted as  $B_z$ ,  $B_\varphi$ ,  $U_z$ , and  $U_\varphi$  respectively. All terms in Equation 5.1 involving the solar



wind velocity,  $\vec{U}$ , and magnetic field were calculated for positions along a specific magnetic field line, using input data from the CME simulation as follows:

- $U_z$  is the radial component of the solar wind velocity at a radial distance from the Sun,  $z$ . This quantity was directly interpolated from Lario's solar wind data. For this and similar quantities, we wrote subroutines to input Lario's data file (735MB) and perform trilinear interpolation over the input grid values in radius, azimuthal angle, and time (see Appendix C).
- $l_z$  is the radial component of the unit vector of the magnetic field at a radial distance from the Sun,  $z$ . This quantity was also directly interpolated from Lario's magnetic field data:

$$\begin{aligned} l_z &= \frac{B_z}{|\vec{B}|} \\ &= \frac{B_z}{\sqrt{B_z^2 + B_\varphi^2}}. \end{aligned} \quad (5.5)$$

- $\vec{U} \cdot \hat{l}$  is the solar wind speed along the magnetic field line:

$$\vec{U} \cdot \hat{l} = U_z l_z + U_\varphi l_\varphi. \quad (5.6)$$

- $l_i l_j (\partial U_j / \partial x_j)$  is the difference in the solar wind speed along the magnetic field line as the radial distance  $z$  changes:

$$l_i l_j \frac{\partial U_j}{\partial x_j} = \frac{\Delta(\vec{U} \cdot \hat{l})}{\Delta z} l_z. \quad (5.7)$$

- $\vec{\nabla} \cdot \vec{U}$  is the divergence of the solar wind velocity:

$$\vec{\nabla} \cdot \vec{U} = \frac{1}{z^2} \frac{\Delta z U_z}{\Delta z} + \frac{1}{z} \frac{\Delta U_\varphi}{\Delta \varphi}. \quad (5.8)$$

- $\hat{l} \cdot \partial \vec{U} / \partial t$  is the change in the solar wind velocity within a small timestep along the magnetic field line:

$$\hat{l} \cdot \frac{\partial \vec{U}}{\partial t} = l_z \frac{\Delta U_z}{\Delta t} + l_\varphi \frac{\Delta U_\varphi}{\Delta t}. \quad (5.9)$$

- $\nabla \cdot \hat{l}$  is the divergence of the magnetic field:

$$\vec{\nabla} \cdot \hat{l} = \frac{1}{z^2} \frac{\Delta(zl_z)}{\Delta z} + \frac{1}{z} \frac{\Delta l_\varphi}{\Delta \varphi}. \quad (5.10)$$

- $\vec{U} \cdot \partial \hat{l} / \partial t$  is the solar wind speed at radial distance  $z$  along the change in magnetic field direction within a small timestep:

$$\vec{U} \cdot \frac{\partial \hat{l}}{\partial t} = U_z \frac{\Delta l_z}{\Delta t} + U_\varphi \frac{\Delta l_\varphi}{\Delta t}. \quad (5.11)$$

The CME simulations consider a generic CME, which should provide us with information on the magnetic field and solar wind nearby the CME and its shock. The model used a method of two-dimensional magnetohydrodynamics (MHD) written in the Fortran language. Spatial domains of interest are from the solar vicinity (18 solar radii or approximately 0.08 AU) to about 430 solar radii or 2 AU and over 180 degrees in the ecliptic plane. The simulation grid spacings are 0.75 degrees and 0.5 solar radii. The CME drove a shock outward from the Sun in the ecliptic plane with a speed of  $4.88 \times 10^{-4}$  AU/min. or approximately 1200 km/s. The simulation time is about 115 hours.

The results were recorded as a binary file (735 MB). We extracted only information we need for our simulations, say, time, position, and radial and angular components of the magnetic field and solar wind. We extract the information into 6 files:

- **bline.dat** (1.1 MB) contains information on radial positions, angular positions of a magnetic field line of interest developed in time and the corresponding radial and angular components of magnetic field and solar wind along the field line as a function of radius. We chose a field line close to the CME in order to obtain clear information about its shock.
- **shock.dat** (1.5 kB) contains the radial position vs. time of the shock driven by the CME.
- **ur.dat** (215 MB) contains the radial component of the solar wind velocity,  $U_z$ , vs. position and time for every magnetic field line developing in time.
- **uh.dat** (222 MB) contains the angular component of the solar wind velocity,  $U_\varphi$ , vs. position and time for every magnetic field line developing in time.
- **br.dat** (215 MB) contains the radial component of the magnetic field,  $B_z$ , vs. position and time for every magnetic field line developing in time.
- **bh.dat** (214 MB) contains the angular component of magnetic field,  $B_\varphi$ , vs. position and time for every magnetic field line developing in time.

These data files are used for calculations of functions in the transport equation (Equation 5.1) as described earlier in this section.

### 5.3.2 Model II

Model II uses the same transport equation, but with the assumption of an Archimedean spiral field (see Figure 2.1) for some quantities. Then some of the terms described above can be written in analytic forms [Ruffolo, 1995] as shown below:

- $l_z$  :

$$l_z = \frac{R}{\sqrt{z^2 + R^2}}, \quad (5.12)$$

where  $R$  is the radial distance from the Sun at which the angle between the magnetic field line and the radial direction is 45 degrees.

- $\vec{\nabla} \cdot \hat{l}$  :

$$\vec{\nabla} \cdot \hat{l} = \frac{R(z^2 + 2R^2)}{z(z^2 + R^2)^{\frac{3}{2}}}. \quad (5.13)$$

- $\vec{\nabla} \cdot \vec{U}$  :

$$\vec{\nabla} \cdot \vec{U} = \frac{2U}{z}. \quad (5.14)$$

### 5.3.3 Program Descriptions

The program is named “fd,” which is an abbreviation of “Forbush decrease”. The purpose of this work is to simulate the first step of a Forbush decrease for a generic CME and its shock. The program comprises 9 files of C source code and 1 file of Fortran source code. It also requires 7 input files:

1. `fd.c`: This is the main program for simulating the transport of energetic charged particles in the heliosphere, including proper treatment of particle motion across a shock. It receives all the input files and calls other subroutines.
2. `field.c`: This file contains all functions related to the magnetic field.
3. `decel.c`: This file is responsible for adiabatic deceleration or acceleration processes. It actually calculates Equation 5.3.

4. `initial.c`: This subroutine contains initial values for the particle density. We set the particle distribution function,  $F$ , to be proportional to the square of the radial distance from the Sun,  $z^2$ , which is appropriate for GCR in the heliosphere.
5. `inject.c`: This file provides an injection of particles during the simulation of the particle transport in case we need one. The current work does not require this feature.
6. `nrutil.c`: This file collects several utility functions modified from the book Numerical Recipes in C [Press et al., 1988].
7. `printout.c`: This file controls the format of our outputs.
8. `stream.c`: This subroutine is responsible for the convection and streaming processes (Equation 5.4).
9. `tridag.c`: This subroutine solves a tridiagonal matrix equation. It was also modified from Press et al. (1988).
10. `muphi.f`: This subroutine was written in Fortran to calculate particle orbits when crossing the shock.

The input files consists of 6 files as described in Section 5.3.1 and one containing the simulation parameters as shown below:

1. `starting time`: 236.2738 min.
2. `stop time`: 499.585975 min.
3. `time step ( $\Delta t$ )`: 0.415975 min.

4. printing time: 41.5975 min.
5. number of  $\mu$ -values (nmu): 15 min.
6. number of momentum values (np): 1
7. momentum values ( $p$ ): 10,897.963 MeV/ $c$  (corresponding to an energy of 10 GeV).
8. lower edge of the spatial domain of simulation (startz): 0.108520 AU.
9. upper edge of the spatial domain of simulation (endz): 0.808520 AU.
10. spatial distance step ( $\Delta z$ ): 0.025 AU.
11. particle rest mass ( $m$ ): 938.28 MeV/ $c^2$  (proton).
12. mean free path of interplanetary scattering ( $\lambda$ ): 0.25 AU. This is consistent with the particle's energy [Bieber et al., 1994].
13. q: 1.0. This quantity characterizes the steepness of a presumed power spectrum of interplanetary magnetic turbulence, which relates to the pitch angle scattering coefficient (see Section 4.2.1).

The starting time, stop time, and spatial domain of the simulation have to be in the domain of Lario's input data. The time step and the spatial distance step are related by  $v\Delta t \approx \Delta z$ , where  $v$  is the particle velocity.

## 5.4 Results and Discussion

In Model I, we encountered a serious problem in that our interpolated function values were highly erratic as a function of radius. After extensive checking, it was determined that our interpolation was correct, but the input values, i.e., output of the CME simulation, were themselves erratic. Since the transport equation requires derivatives of  $\vec{U}$  and  $\vec{B}$ , it is necessary to use smooth input values of  $\vec{U}$  and  $\vec{B}$ .

Therefore, we have instead used Model II replacing some of the erratic values based on CME simulation output with idealized theoretical values to generate the results shown in this section, which are able to qualitatively simulate the Forbush decrease phenomenon.

Figure 5.2 shows the particle distribution function vs. radial distance from the Sun. Each line represents  $F$  at a different time. The vertical dashed lines represent the positions of the shock for different times. The left side of the shock is downstream; the right side of the shock is upstream. As shown in the figure,  $F$  decreases just downstream as a result of reflection at the shock. The decrease obviously begins just upstream of the shock, which is known as the loss cone effect as discussed earlier in Chapter 4. We can compare with the FD observation during days of year (DOY) 239 to 240 in the year 2001 as shown in Figure 5.3 (see also Chapter 3 and Figure 3.3). The results are slightly different from the observations. First, the second step of the Forbush decrease does not appear in our results because it results from a different mechanism that is intentionally not taken into account in this work. (It results from cross-field diffusion into the CME ejecta, which is not treated by our transport model.) Second, the decrease in the observation appears to be steeper. This is because



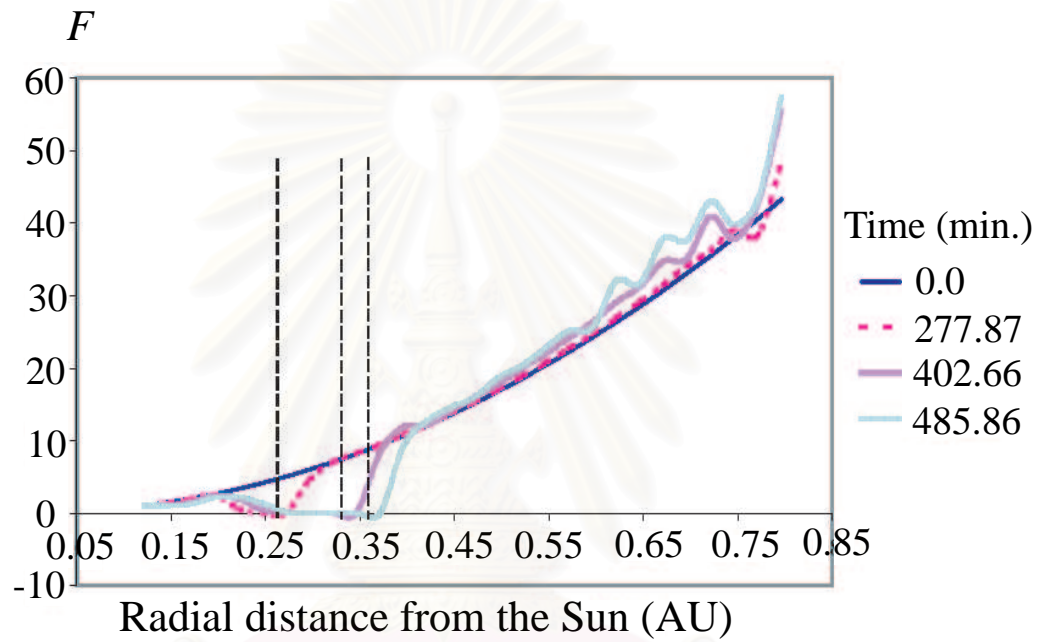


Figure 5.2: The simulation results of Forbush decrease.

สถาบันวิทยบริการ  
จุฬาลงกรณ์มหาวิทยาลัย

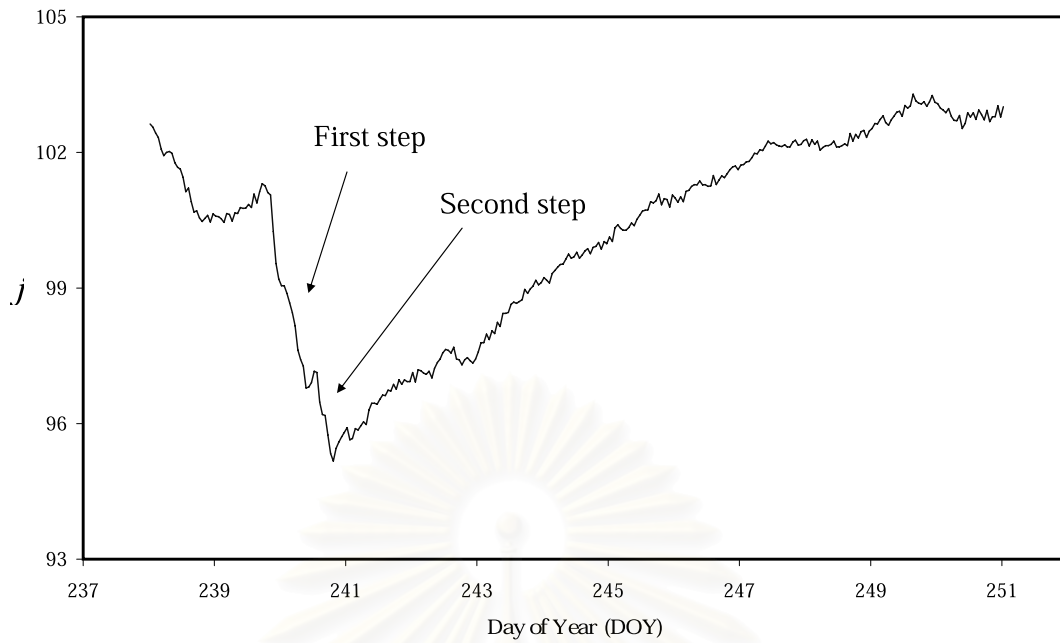


Figure 5.3: Observation of a Forbush decrease during DOY 239 to 240 in the year 2001. [Data provided by J. W. Bieber, 2003.]

the figures are set to different scales and the particle density in our simulation is strictly along a magnetic field line while the observation represents CR particles coming from a certain direction in space for a fixed observer. Third, the upstream region is to the right of the shock (higher  $z$ ) in Figure 5.2, while it is on the left side in Figure 5.3, corresponding to earlier times before the shock flows past the fixed observer. This point is also demonstrated in Figure 2.8 and 2.9. In any case, the Forbush decrease is clearly demonstrated in our results.

สถาบันวิทยบริการ  
จุฬาลงกรณ์มหาวิทยาลัย

# References

- Abraham-Shrauner, B. Determination of magnetohydrodynamics shock normal, J. Geophys. Res. **77** (1972): 736.
- Barnden, L. R., Forbush decreases 1966-1972: Their solar and inter-planetary associations and their anisotropies, Proc. 13<sup>th</sup> Intl. Cosmic Ray Conf., **2** (1973): 1271.
- Belov, A. V., Bieber, J. W., Eroshenko, E. A., Evenson, P., Pyle, R., and Yanke, V. G., Pitch-angle features in cosmic rays in advance of severe magnetic storms: Neutron monitor observations, Proc. 27<sup>th</sup> Intl. Cosmic Ray Conf., **9** (2001): 3507.
- Belov, A. V., Dorman, L. I., Eroshenko, E. A., Iucci, N. Villorosi, G. and Yanke, V. G., Search for predictors of Forbush decreases, Proc. 24<sup>th</sup> Intl. Cosmic Ray Conf., **1** (1995): 888
- Bieber, J. W., Chen, J., Matthaeus, W. H., Smith, C. W., and Pomerantz, M. A., Long-term variations of interplanetary magnetic field spectra with implications for cosmic ray modulation, J. Geophys. Res., **98** (1993): 3585.
- Bieber, J. W., and Evenson, P., CME geometry in relation to cosmic ray anisotropy, Geophys. Res. Lett., **25** (1998): 2955.
- Bieber, J. W., Evenson, P., Dröge, W., Pyle, R., Ruffolo, D., Rujiwarodom, M., Tooprakai, P., and Khumlumlert, T., Spaceship Earth Observations of the Easter 2001 solar particle event, Astrophys. J. Lett., **601** (2004): L103.
- Bieber, J. W., Matthaeus, W. H., Smith, C. W., Wanner, W., Kallenrode, M.-B., and Wibberenz, G., Proton and electron mean free paths: The Palmer consensus revisited, Astrophys. J., **420** (1994): 294.
- Bieber, J. W., and Pomerantz, M. A., A unified theory of cosmic ray diurnal variations, Geophys. Res. Lett., **10** (1983): 920.

- Brueckner, G. E., Delaboudiniere, J.-P., Howard, R. A., Paswaters, S. E., St. Cyr, O. C., Schwenn, R., Lamy, P., Simnett, G. M., Thompson, B., and Wang, D., Geomagnetic storms caused by coronal mass ejections (CMEs): March 1996 through June 1997, Geophys. Res. Lett., **25** (1998): 3019.
- Burlaga, L. F., Interplanetary Magnetohydrodynamics, Oxford University Press, 1995.
- Cane, H. V., Energetic particles in the solar wind: Propagation, acceleration, and modulation, Proc. 25<sup>th</sup> Intl. Cosmic Ray Conf., **8** (1997): 135.
- Cane, H. V., Coronal mass ejections and Forbush decreases, Space Sci. Rev., **93** (2000): 55.
- Cane, H. V., Richardson, I. G., von Roseninge, T. T., and Wibberenz, G., Cosmic ray decreases and shock structure: A multispacecraft study, J. Geophys. Res., **99** (1994): 21429.
- Cane, H. V., Wibberenz, G., and Richardson, I. G., Solar magnetic field variations and cosmic ray modulation, Proc. Solar Wind 9, **471** (1999): 99.
- Cane, H. V., Wibberenz, G., Richardson, I. G., and von Roseninge, T. T., Cosmic ray modulation and the solar magnetic field, Geophys. Res. Lett., **26** (1999): 565.
- Chen, J., and Bieber, J. W., Cosmic-ray anisotropies and gradients in three dimensions, Astrophys. J., **405** (1993): 375.
- Cliwer, E. W., Droege, W., and Mueller-Mellin, R., Superevents and cosmic ray modulation, 1974- 1985, J. Geophys. Res., **98** (1993): 15231.
- Colburn, D. S., and Sonett, C. P., Discontinuity in the solar wind, Space Sci. Rev., **5** (1996): 435.
- Compton, A. H., and Getting, I. A., An apparent effect of galactic rotation on the intensity of cosmic rays, Phys. Rev., **47** (1935): 817.
- Cravens, T. E., Physics of solar system plasmas, New York: Cambridge University Press, 1997.

- de Hoffmann, F., and Teller, E. Magneto-hydrodynamic shocks, Phys. Rev. **80** (1950): 692.
- Dorman, V. L., Iucci, N., and Villaresi, G., The nature of cosmic ray Forbush-decrease and precursory effects, Proc. 24<sup>th</sup> Intl. Cosmic Ray Conf., **4** (1995): 892.
- Forman, M. A., The Compton-Getting effect for cosmic-ray particles and photons and the Lorentz-invariance of distribution functions, Planetary and Space Sci., **18** (1970): 25.
- Friedlander, M. W., Cosmic Rays, Harvard University Press, 1989.
- Gleeson, L. J., and Axford, W. I., The Compton-Getting effect, Astrophys. Space Sci., **2** (1968): 431.
- Gosling, J. T., Coronal mass ejections and magnetic flux ropes in interplanetary space, in Physics of magnetic flux ropes, Washington, DC: Amer. Geophys. Union (1990): 343.
- Gosling, J. T., Baker, D. N., Bame, S. J., Feldman, W. C., Zwickl, R. D., and Smith, E. J., Bidirectional solar wind electron heat flux events, J. Geophys. Res., **92** (1987): 8519.
- Gosling, J. T., Bame, S. J., McComas, D. J., and Phillips, J. L., Coronal mass ejections and large geomagnetic storms, Geophys. Res. Lett., **17** (1990): 901.
- Gosling, J. T., Birn, J., McComas, D. J., Phillips, J. L., and Hesse, M., Open and disconnected magnetic field lines within coronal mass ejections in the solar wind: Evidence for 3-dimensional reconnection, Proc. Solar Wind 8 (1995): 46.
- Hall, D. L., Duldig, M. L., and Humble, J. E., Cosmic-ray modulation parameters derived from the solar diurnal variation, Astrophys. J., **482** (1997): 1038.
- Hundhausen, A. J., The origin and propagation of coronal mass ejections, Proc. Solar Wind 6, **1** (1988): 181.

- Ihara, A., Doke, T., Hasebe, N., Kikuchi, J., Kobayashi, M.-N., Maezawa, K., Nagata, K., Sakaguchi, T., Shino, T., Takashima, T., Teruhi, S., Wilken, B., and Yanagimachi, T., Electron and ion spectrometer (EIS) on board in the Nazomi spacecraft, Proc. 27<sup>th</sup> Intl. Cosmic Ray Conf., **8** (2001): 3429.
- Iucci, N., Parisi, M., Storini, M., and Villoresi, G., Forbush decreases - Origin and development in the interplanetary space, Nuovo Cimento C, **2C** (1979): 1.
- Jokipii, J. R., Cosmic-ray propagation. I. Charged particles in a random magnetic field, Astrophys. J., **146** (1966): 480.
- Jokipii, J. R., Propagation of cosmic rays in the solar wind, Rev. Geophys. Space Phys., **9** (1971): 27.
- Kirk, J. G., Pitch-angle anisotropy of low-energy ions at interplanetary shocks, Astrophys. J., **324** (1988): 557.
- Kirk, J. G., Melrose, D. B., and Priest, E. R., Plasma Astrophysics, Springer-Verlag, 1994.
- Kirk, J. G., and Schneider, P., Hydromagnetic constraints on deep zonal flow in the giant planets, Astrophys. J., **315** (1987): 425.
- Kolomeets, E. V., Sergeeva, G. A., Nemolochnov, A. N., Chumbalova, R. A., and Zusmannovich, A. G., Periodic cosmic ray variations and their change during the cycle of solar activity, Proc. 9<sup>th</sup> Intl. Cosmic Ray Conf., **1** (1965): 224.
- le Roux, J. A., and Potgieter, M. S., The simulation of Forbush decreases with time-dependent cosmic-ray modulation models of varying complexity, Astron. Astrophys., **2** (1991): 531.
- Leerunnavarat, K., Ruffolo, D., and Bieber, J. W., Loss cone precursors to Forbush decreases and advance warning of space weather effects, Astrophys. J., **593** (2003): 587.
- Leerunnavarat, K., Sanguansak, N., and Ruffolo, D. A hybrid orbit-finite difference



method for simulating the shock acceleration of cosmic rays, The 4<sup>th</sup> Ann. Nat. Symp. on Comp. Sci. and Eng., 2000.

Lockwood, J. A., Forbush decreases in the cosmic radiation, Space Sci. Rev., **12** (1971): 6011.

Lockwood, J. A., Webber, W. R., Jokipii, J. R., Characteristic recovery times of Forbush-type decreases in the cosmic radiation. I - Observations at earth at different energies, J. Geophys. Res., **91** (1986): 2851.

Morishita, I., Fujimoto, K., Fujii, Z., Sakakibara, S., Nagashima, K., Munakata, K., Yasue, S., Humble, J. E., Fenton, A. G., and Duldig, M. L., Characteristics of precursory decrease of Forbush decrease inferred from world wide observations of muon and neutron intensities, Proc. 25<sup>th</sup> Intl. Cosmic Ray Conf., **1** (1997): 405.

Morishita, I., Nagashima, K., Sakakibara, S., and Munakata, K., Long term changes of the rigidity spectrum of Forbush decrease, Proc. 21<sup>st</sup> Intl. Cosmic Ray Conf., **6** (1990): 217.

Munakata, K., Bieber, J. W., Kuwabara, T., Hattori, T., Inoue, K., Yasue, S., Kato, C., Fujii, Z., Fujimoto, K., Duldig, M. L., Humble, J. E., Trivedi, N. B., Gonzalez, W. D., Silva, M. R., Tsurutani, B. T., and Schuch, N. J., A prototype muon detector network covering a full range of cosmic ray pitch angles, Proc. 27<sup>th</sup> Intl. Cosmic Ray Conf., **9** (2001): 3494.

Munakata, K., Bieber, J. W., Yasue, S., Kato, C., Koyama, M., Akahane, S., Fujimoto, K., Fujii, Z., Humble, J. E., and Duldig, M. L., Precursors of geomagnetic storms observed by the muon detector network, J. Geophys. Res., **105** (2000): 27457.

Nagashima, K., Fujimoto, K., and Morishita, I., Interplanetary magnetic field collimated cosmic ray flow across magnetic shock from inside of Forbush decrease, observed as local-time dependent precursory decrease on the ground,



- J. Geophys. Res., **99** (1994): 21419.
- Nagashima, K., Fujimoto, K., Sakakibara, S., and Morishita, I., Local-time-dependent pre-IMF-shock decrease and post-shock increase of cosmic rays, produced respectively by their IMF-collimated outward and inward flows across the shock responsible for Forbush decrease, Planet. Space. Sci., **40** (1992): 1109.
- Ng, C. K., and Wong, K.-Y., Solar particle propagation under the influence of pitch-angle diffusion and collimation in the interplanetary magnetic field, Proc. 16<sup>th</sup> Intl. Cosmic Ray Conf., **5** (1979): 252.
- Nutaro, T., Riyavong, S., and Ruffolo, D. Application of a generalized total variation diminishing algorithm to cosmic ray transport and acceleration, Computer Physics Communications, **134** (2001): 209.
- Parks, G. K. Physics of space plasmas: An introduction, Washington: Addison-Wesley Publishing Company, 1991.
- Parker, E. N., Interplanetary Dynamical Processes, Interscience Publishing, 1963.
- Press, W. H., Flannery, B. P., Teukolsky, S. A., and Vetterling, W. T., Numerical Recipes in C, Cambridge University Press, 1988.
- Richardson, I. G., and Reames, D. V., Bidirectional about 1 MeV/amu ion intervals in 1973-1991 observed by the Goddard Space Flight Center instruments on IMP 8 and ISEE 3/ICE, Astrophys. J. Suppl. Series, **85** (1993): 411.
- Ridpath, I. Oxford Dictionary of Astronomy, Oxford University Press, 1997.
- Ruffolo, D. Effect of adiabatic deceleration on the focused transport of solar cosmic rays, Astrophys. J., **442** (1995): 861.
- Ruffolo, D. Transport and acceleration of energetic charged particles near an oblique shock, Astrophys. J., **515** (1999): 787.
- Ruffolo, D., and Chuychai P. First-order Fermi acceleration at a continuous compression, Proc. 26<sup>th</sup> Intl. Cosmic Ray Conf., **6** (1999): 552.
- Russell, C. T., Solar wind and interplanetary magnetic field: A tutorial, Space Weather, 2001.

- Sanguansak, N. and Ruffolo, D. A hybrid orbit-finite difference treatment of oblique shock acceleration, Proc. 26<sup>th</sup> Intl. Cosmic Ray Conf., **4** (1999): 459.
- Schlickeiser, R., Cosmic Ray Astrophysics, Berlin, Springer-Verlag, 2002.
- Schwenn, R., Direct correlations between coronal transients and interplanetary disturbances, Space Sci. Rev., **34** (1983): 85.
- Skilling, J. Cosmic ray streaming-I. Effect of Alfvén waves on particles, Mon. Not. R. Astr. Soc., **172** (1975): 557.
- Spreiter, J. R., Summers, A. L., and Alksne, A. Y., Hydromagnetic flow around the magnetosphere, Planet. Space Sci., **14** (1966): 223.
- van Allen, J. A., and Mihalov, J. D., Forbush decreases and particle acceleration in the outer heliosphere, Geophys. Res. Lett., **17** (1990): 761.
- Vandas, M., Fischer, S., Dryer, M., Smith, Z., and Detman, T., Simulation of magnetic cloud propagation in the inner heliosphere in two-dimensions: 1. A loop perpendicular to the ecliptic plane, J. Geophys. Res., **100** (1995): 12285.
- Wibberenz, G., Cane, H. V., and Richardson, I. G., Two-step Forbush decreases in the inner solar system and their relevance for models of transient disturbances, Proc. 25<sup>th</sup> Intl. Cosmic Ray Conf., **1** (1997): 397.
- Wibberenz, G., le Roux, J. A., Potgieter, M. S., and Bieber, J. W., Transient effects and disturbed conditions, Space Sci. Rev., **83** (1998): 309.
- Yanenko, N. N., The Method of Fractional Steps, Springer-Verlag, 1971.
- Zhang, M., McKibben, R. B., Jokipii, J. R., and Rassoul, H. K., Perpendicular transport of solar energetic particles: Ulysses observations at high heliographic latitudes, AGU Fall Meeting, **SH72B-05** (2002).

# Appendix A

## List of Acronyms

ACE	.....	Advanced Composition Explorer
AU	.....	Astronomical Unit
BDE	.....	Bidirectional Solar Wind Electron Heat Flux
BIF	.....	Bidirectional Ion Flows
CME	.....	Coronal Mass Ejection
CR	.....	Cosmic Rays
dHT	.....	de Hoffman-Teller
DOY	.....	Day of Year
EGCR	.....	Extra-Galactic Cosmic Rays
FD	.....	Forbush Decrease
GCR	.....	Galactic Cosmic Rays
GMIR	.....	Global Merged Interaction Region
GV	.....	Gigavolts
HCS	.....	Heliospheric Current Sheet
IMF	.....	Interplanetary Magnetic Field
L1	.....	Inner Sun-Earth Lagrangian Point
MD	.....	Muon Detector

MHD	.....	Magnetohydrodynamics
NM	.....	Neutron Monitor
SEP	.....	Solar Energetic Particles



สถาบันวิทยบริการ  
จุฬาลงกรณ์มหาวิทยาลัย

# Appendix B

## The Relations between $F$ , $f$ , $j$ and $N$

The phase space density is the number of particles in a small 6-dimensional volume of phase space at position  $\vec{x}$  and momentum  $\vec{p}$  at a time of interest,  $t$ . It is written as:

$$f(\vec{x}, \vec{p}, t) = \frac{d^6 N}{d^3 x d^3 p}, \quad (\text{B.1})$$

where  $d^6 N$  is the number of particles in the small 6-dimensional volume  $d^3 x d^3 p$ .

We can also write momentum space of Equation A.1 in spherical coordinates:

$$f = \frac{d^6 N}{d^3 x p^2 dp d\Omega}, \quad (\text{B.2})$$

where  $\Omega$  is a solid angle in momentum (direction) space. Then, we multiply Equation A.2 by  $p^2$ :

$$p^2 f = \frac{d^6 N}{d^3 x dp d\Omega}, \quad (\text{B.3})$$

and use the chain rule to convert from “ $dp$ ” to “ $dE$ ,” where  $E$  is the kinetic energy of a particle. Therefore, Equation A.3 becomes:

$$p^2 f = \frac{d^6 N}{d^3 x dE d\Omega} \frac{dE}{dp}. \quad (\text{B.4})$$

We could find  $dE/dp$  as follows:

$$\begin{aligned}
 E_{total}^2 &= p^2 c^2 + m^2 c^4 \\
 2E_{total} dE_{total} &= 2p dp c^2 \\
 \frac{dE_{total}}{dp} &= \frac{pc^2}{E_{total}} \\
 &= \frac{\gamma m v c^2}{\gamma m c^2} \\
 &= v.
 \end{aligned} \tag{B.5}$$

From

$$\begin{aligned}
 E_{total} &= E + mc^2 \\
 \frac{dE_{total}}{dp} &= \frac{dE}{dp}.
 \end{aligned}$$

Hence,

$$\frac{dE}{dp} = v, \tag{B.6}$$

where  $E_{total}$  is the total energy of a particle,  $mc^2$  is the rest mass energy,  $\gamma$  is the Lorentz factor, and  $v$  is the particle's speed. Then, Equation A.4 becomes:

$$\begin{aligned}
 p^2 f &= v \frac{d^6 N}{d^3 x dE d\Omega} \\
 &= j,
 \end{aligned} \tag{B.7}$$

where  $j$  can be interpreted as a flux of particles ( $\text{s}^{-1}\text{cm}^{-2}\text{sr}^{-1}\text{MeV}^{-1}$ ). This is an important quantity for expressing experimental results.

Assuming that  $j$  is uniform across a cross-sectional area  $A$  and over gyrophase  $\varphi$ , we now multiply  $j$  with  $2\pi A(z)$ , where  $A(z)$  is the cross-section area of a flux tube at a position  $z$  along the tube:

$$2\pi A(z)j = \int \int j dA d\varphi$$

$$\begin{aligned}
&= \int \int \frac{d^6 N}{dz dA dp d\mu d\varphi} dA d\varphi \\
&= \frac{d^3 N}{dz d\mu dp} \\
&= F,
\end{aligned} \tag{B.8}$$

where  $\mu$  is the cosine of pitch angle.  $F$  is called the particle distribution function, which is the number of particles in the small 3-dimensional volume  $dz dp d\mu$ . The quantity  $F$  allows us to use the numerical method of finite differencing to guarantee the conservation of particle number in our transport equation.



สถาบันวิทยบริการ  
จุฬาลงกรณ์มหาวิทยาลัย



# Appendix C

## Operator Splitting Technique

Suppose we have an initial value equation of the form

$$\frac{\partial u}{\partial t} = \mathcal{L}_1 u + \mathcal{L}_2 u + \cdots + \mathcal{L}_m u, \quad (\text{C.1})$$

where  $\mathcal{L}_i$  are some linear operators. Suppose that for each of the terms, we already know a differencing scheme for updating the variable  $u$  from timestep  $n$  to timestep  $n + 1$ , valid if that piece of the operator were the only one on the right-hand side. We will write these updating symbolically as

$$u^{n+1} = \mathcal{U}_1(u^n, \Delta t)$$

$$u^{n+1} = \mathcal{U}_2(u^n, \Delta t)$$

...

...

$$u^{n+1} = \mathcal{U}_m(u^n, \Delta t).$$

(C.2)

Now, one form of operator splitting would be to get from  $n$  to  $n + 1$  by the following sequence of updates:

$$\begin{aligned}
u^{n+(1/m)} &= \mathcal{L}_1(u^n, \Delta t) \\
u^{n+(2/m)} &= \mathcal{L}_2(u^{n+(1/m)}, \Delta t) \\
&\dots \\
&\dots \\
u^{n+1} &= \mathcal{L}_m(u^{n+(m-1)/m}, \Delta t).
\end{aligned} \tag{C.3}$$

Therefore, this method allows us to efficiently solve an equation containing various terms, e.g., corresponding to various physical processes.



สถาบันวิทยบริการ  
จุฬาลงกรณ์มหาวิทยาลัย

# Vitae

Name: Kanokporn Leerunnavarat

Born: June 3<sup>rd</sup>, 1974

Address: 15/323 Chokechai 4 soi 14 Ladprao, Bangkok, Thailand

## International Publications:

1. Leerunnavarat, K., Ruffolo, D., Bieber, J. W., "Loss Cone Precursors to Forbush Decreases and Advance Warning of Space Weather Effects", *Astrophys. J.*, 593 (2003): 587.

## Conference Presentations:

1. Leerunnavarat, K., Sanguansak, N., Ruffolo, D., "A Hybrid Orbit-Finite Difference Method for Simulating the Shock Acceleration of Cosmic Rays", The Fourth Annual National Symposium on Computational Science and Engineering, (Thailand, March, 2000).
2. Leerunnavarat, K., Ruffolo, D., Bieber, J. W., "Precursors to Forbush Decreases and Advanced Warning of Space Weather Effects", The 26<sup>th</sup> Congress on Science and Technology of Thailand, (Thailand, October, 2000).
3. Leerunnavarat, K., Ruffolo, D., Bieber, J. W., "Loss Cone Precursors of CME Shocks", AGU 2000 Fall Meeting, (San Francisco, USA, December, 2000).
4. Leerunnavarat, K., Ruffolo, D., Bieber, J. W., "Precursors to Forbush Decreases and Advanced Warning of Space Weather Effects", The 9<sup>th</sup> Annual University Meeting of Science, Chulalongkorn University, Bangkok, (Thailand, March, 2001).
5. Leerunnavarat, K., Ruffolo, D., Bieber, J. W., "Precursors to Forbush Decreases and Advanced Warning of Space Weather Effects", RGJ – PhD Congress II, (Thailand, April, 2001).
6. Klappong, K., Leerunnavarat, K., Chuychai, P., Hirunsirisawat, E., Ruffolo, D., "Comparison between Particle Acceleration at a Continuous Compression and at a Shock", The Fifth Annual National Symposium on Computational Science, Engineering, (Thailand, June, 2001).
7. Klappong, K., Leerunnavarat, K. (presenter), Chuychai, P. and Ruffolo, D., "Particle Acceleration and Pitch Angle Transport near a Thin Shock and a Compression Region, and a Structured Shock," *Proc. 27th Internat. Cosmic Ray Conf.*, 8, 3461 (Germany, August, 2001).
8. Klappong, K., Leerunnavarat, K., Chuychai, P., Ruffolo, D., "Particle Acceleration and Pitch Angle Transport near a Thin Shock and a Compression Region", The 27<sup>th</sup> Congress on Science and Technology of Thailand, (Thailand, October, 2001).
9. Leerunnavarat, K., Ruffolo, D., Bieber, J. W., "Cosmic Ray Anisotropy Near a CME-Driven Shock", AGU 2002 Spring Meeting, (USA., May 2002).
10. Malakit, K., Klappong, K., Leerunnavarat, K., Ruffolo, D., "Particle Acceleration at Regions Near Shocks and Plasma Compressions for Various Angles Between the Magnetic Field and Shock Normal", The 28<sup>th</sup> Congress on Science and Technology of Thailand, (Thailand, October, 2002).
11. Malakit, K., Klappong, K., Leerunnavarat, K. and Ruffolo, D., "Effects of Systematic Pitch-Angle Changes on Cosmic Ray Acceleration on Shocks and Compression Regions: Contribution of the Mirroring Effect," *Proc. 7th Ann. Natl. Symp. Computational Sci. and Eng. (Thailand)* (Bangkok, March, 2003)
12. Malakit, K., Klappong, K., Leerunnavarat, K., Chuychai, P., Sanguansak, N. and Ruffolo, D., "Particle Acceleration at Fluid Compressions and What That Teaches Us about Shock Acceleration," *Proc. 28th Internat. Cosmic Ray Conf.*, 6, 3677 (Japan, August, 2003).